![NASA logo]

High Speed Inlet Distortion Test for the X–59 Low Boom Flight Demonstrator in the NASA Glenn 8- by 6-Foot Supersonic Wind Tunnel

Vance F. Dippold III
Glenn Research Center, Cleveland, Ohio

NASA STI Program . . . in Profile

Since its founding, NASA has been dedicated to the advancement of aeronautics and space science. The NASA Scientific and Technical Information (STI) Program plays a key part in helping NASA maintain this important role.

The NASA STI Program operates under the auspices of the Agency Chief Information Officer. It collects, organizes, provides for archiving, and disseminates NASA's STI. The NASA STI Program provides access to the NASA Technical Report Server—Registered (NTRS Reg) and NASA Technical Report Server—Public (NTRS) thus providing one of the largest collections of aeronautical and space science STI in the world. Results are published in both non-NASA channels and by NASA in the NASA STI Report Series, which includes the following report types:

- TECHNICAL PUBLICATION. Reports of completed research or a major significant phase of research that present the results of NASA programs and include extensive data or theoretical analysis. Includes compilations of significant scientific and technical data and information deemed to be of continuing reference value. NASA counter-part of peer-reviewed formal professional papers, but has less stringent limitations on manuscript length and extent of graphic presentations.

- TECHNICAL MEMORANDUM. Scientific and technical findings that are preliminary or of specialized interest, e.g., "quick-release" reports, working papers, and bibliographies that contain minimal annotation. Does not contain extensive analysis.

- CONTRACTOR REPORT. Scientific and technical findings by NASA-sponsored contractors and grantees.

- CONFERENCE PUBLICATION. Collected papers from scientific and technical conferences, symposia, seminars, or other meetings sponsored or co-sponsored by NASA.

- SPECIAL PUBLICATION. Scientific, technical, or historical information from NASA programs, projects, and missions, often concerned with subjects having substantial public interest.

- TECHNICAL TRANSLATION. English-language translations of foreign scientific and technical material pertinent to NASA's mission.

For more information about the NASA STI program, see the following:

- Access the NASA STI program home page at http://www.sti.nasa.gov

- E-mail your question to help@sti.nasa.gov

- Fax your question to the NASA STI Information Desk at 757-864-6500

- Telephone the NASA STI Information Desk at 757-864-9658

- Write to:
  NASA STI Program
  Mail Stop 148
  NASA Langley Research Center
  Hampton, VA 23681-2199

High Speed Inlet Distortion Test for the X–59 Low Boom Flight Demonstrator in the NASA Glenn 8- by 6-Foot Supersonic Wind Tunnel

Vance F. Dippold III
Glenn Research Center, Cleveland, Ohio

Acknowledgments

Level of Review: This material has been technically reviewed by technical management.

High Speed Inlet Distortion Test for the X–59 Low Boom Flight Demonstrator in the NASA Glenn 8- by 6-Foot Supersonic Wind Tunnel

Vance F. Dippold III
National Aeronautics and Space Administration
Glenn Research Center
Cleveland, Ohio 44135

Abstract

The Low Boom Flight Demonstrator (LBFD) High Speed Inlet Distortion Test (HSIDT) was completed in the NASA Glenn Research Center 8- by 6-Foot Supersonic Wind Tunnel (8x6 SWT) using a 9.5 percent-scale propulsion model of the X–59 to evaluate the compatibility and operability of the inlet and engine integration, focusing on the inlet dynamic effects at the engine face. The model was instrumented with steady-state and high-response total pressure probes in the conventional 40-point, equal-area array at the aerodynamic interface plane (AIP). The HSIDT successfully collected high-response distortion data points for the X–59 from Mach = 0 to 1.55 for a wide range of angle-of-attack, angle-of-sideslip, and inlet flow. Analyses showed that inlet dynamic distortion and inlet planar wave (or inlet buzz) were within engine limits through most of the flight envelope. The test data showed that inlet planar wave was present at Mach 1.35 and above, at airflows between idle and maximum engine airflow. Engine throttle back will need to be limited when decelerating from supersonic flight Mach to avoid these regions of inlet planar wave. The HSIDT data was also used to compare the metric SUM40, computed from the 40 high-response AIP total pressure probes, with the metric SUM4, computed from four high-response inlet static pressure probes. The data showed that SUM4 can be used as a surrogate for SUM40 during the X–59 flight test to detect inlet planar wave.

Nomenclature

α	Angle-of-attack
AIP	Aerodynamic interface plane; located at engine face
β	Angle-of-sideslip
Fs	High-response sampling frequency, 20,000 Hz
HR	High-response
i	High-response scan index
IDCMAX	General Electric circumferential distortion parameter
IDRMAX	General Electric radial distortion parameter
M	Freestream Mach number
m_2/m_0	Inlet mass flow ratio
NSCAN	Total number of high-response scans per reading; 60,000 scans
p_{s2}	Inlet static pressure, just upstream of AIP; four probes, area-averaged
p_{t2}	Inlet total pressure at AIP; 40 probes, area-averaged
p_{t2}/p_{t0}	Inlet total pressure recovery; 40 probes, area-averaged
PSD	Power spectral density

SUM40	Inlet planar wave indicator using the root-mean-square of the instantaneous total pressure recoveries from 40 AIP high-response total pressure probes
SUM4	Inlet planar wave indicator using the root-mean-square of the instantaneous static pressures from four inlet high-response static pressure probes
SS	Steady-state

Subscripts

| dynamic | Instantaneous value of high-response measurement |
| mean | Time-mean value of high-response measurement |

1.0   Introduction

It is well known that one of the greatest challenges for overland public supersonic flight in the USA is that supersonic aircraft produce sonic booms that are disruptive to observers on the ground. In recent years, NASA and numerous other organizations have made substantial investments to understand sonic boom propagation and to develop technologies to design supersonic aircraft that reduce the annoyance of the sonic boom for ground-based observers. NASA is building a new X-plane—the X–59 "QueSST" Low Boom Flight Demonstrator—that is designed to produce a sonic "thump" at its supersonic cruise speed. The X–59 will be used to validate quiet sonic boom design technologies. Additionally, the X–59 will be flown over actual communities at approximately Mach 1.40 to collect community response data that will be reported to the International Civil Aviation Organization (ICAO) in an effort to change the current overland public supersonic flight restriction. While future commercial supersonic transport aircraft will be significantly larger than the X–59, the sound pressure level of the sonic thumps produced by the X–59 will be representative of those produced by future supersonic transport aircraft.

The X–59 demonstrator aircraft (pictured in Figure 1) is approximately 96.67 ft long, with a wingspan of about 30 ft. The design Mach number is 1.40, though the aircraft will be flown at slightly higher Mach numbers during flight testing. Every design decision was made to help the aircraft meet its design sonic

Figure 1.—Artist rendering of the X–59 Low Boom Flight Demonstrator.

boom levels (approximately 75 PLdB). The X–59's propulsion system is top-mounted, using the airframe to shield the ground from shockwaves produced by the inlet and nozzle. At first glance, the integrated inlet and propulsion system looks unfavorable: upstream of the inlet is a long length of fuselage with an external camera fairing upstream of the cockpit, vortex generators just downstream of the cockpit, and environmental control system inlets and exhaust vents on the upper surface of the wings. Ordinarily, the engine would be susceptible to performance-robbing boundary layer flow. However, the X–59 uses a diverterless bump inlet, in which the bump acts as a compression surface to divert the boundary layer outboard.

The QueSST Inlet Performance Test (Ref. 1) was conducted in the NASA Glenn Research Center 8- by 6-Foot Supersonic Wind Tunnel (8x6 SWT) in 2017 to assess the performance of the X–59's diverterless bump inlet. The 9.5 percent-scale Inlet Performance Test model was instrumented with a 40-probe steady-state total pressure array at the aerodynamic interface plane (AIP), located near the engine face. Inlet mass flow was controlled with a calibrated parabolic mass flow plug downstream of the AIP. The Inlet Performance Test found the inlet to perform close to predictions in terms of inlet total pressure recovery. However, steady-state inlet distortion levels were high enough that a dynamic inlet distortion test was required to assess inlet-engine compatibility and operability.

In 2019, the QueSST High Speed Inlet Distortion Test (HSIDT) was conducted in the 8x6 SWT. The primary objective of the second test was to evaluate the compatibility and operability of the integrated inlet and engine, focusing on the inlet dynamic effects at the engine face. The secondary objectives of the inlet distortion test included evaluating performance of the latest design iteration of the inlet and analyzing the effects of recent geometry changes to the aircraft design.

2.0   Experimental Setup

2.1   NASA Glenn Research Center 8- by 6-Foot Supersonic Wind Tunnel

The HSIDT was performed in the 8x6 SWT (Refs. 2 to 4). The 8x6 SWT is an atmospheric wind tunnel, able to operate from Mach 0.26 to 2.0. The facility is capable of operation in either an aerodynamic (closed-loop) cycle or a propulsion (open-loop) cycle. During the HSIDT, the tunnel operated in a closed-loop cycle. The test section is 8 ft high, 6 ft wide, 23.5 ft long and is contained within a pressure-regulated balance chamber. The initial 9 ft of the test section, known as the supersonic test section, is surrounded by solid walls. Downstream of this, in the transonic test section, all four walls are perforated with 1-in.-diameter holes designed to mitigate wave reflections during transonic testing (Ref. 5). Several configurations of holes are available. This test used the 5.8 percent porosity configuration.

While the design cruise Mach number of the X–59 is Mach = 1.40, the 8x6 SWT is calibrated for discrete Mach numbers. The HSIDT bracketed the design cruise Mach with the closest 8x6 SWT calibrated tunnel Mach numbers, Mach = 1.35 and 1.45. This report will refer to Mach = 1.45 as the "cruise" Mach number for HSIDT.

2.2   Wind Tunnel Model

2.2.1   QueSST Propulsion Model

A 9.5 percent-scale model of the X–59 aircraft was tested, as shown in Figure 2. The propulsion model included the X–59 airframe from the nose to just downstream of the inlet, including the fuselage, canards, and wings—the model did not include the vertical tail or horizontal stabilizers. The model was
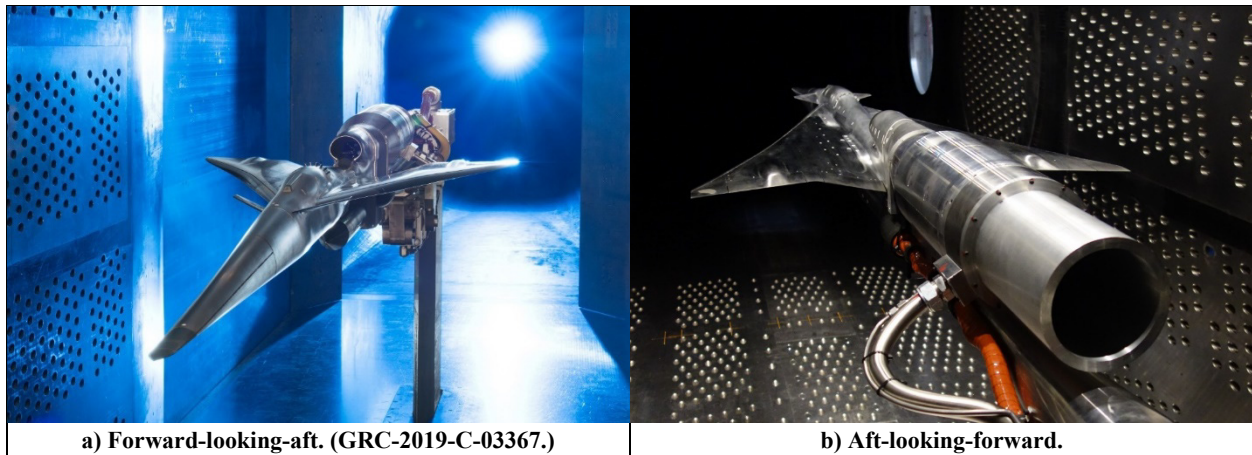
| a) Forward-looking-aft. (GRC-2019-C-03367.) | b) Aft-looking-forward. |

Figure 2.—The 9.5 percent-scale propulsion model of the X–59 used for High Speed Inlet Distortion Test.

attached to a sting, which was mounted to the wind tunnel's strut. The HSIDT reused much of the model hardware used in the 2017 QueSST Inlet Performance Test, in which the X–59 configuration, denoted C607, was examined (Ref. 1). The 2017 Inlet Performance Test also tested a revised inlet, from the C608 configuration, on the C607 body (the C608 inlet throat area was approximately 3.5 percent larger than that of the C607). The C607 model was significantly updated for the 2019 HSIDT to represent design elements from the more recent C611 configuration. The C611 inlet throat area was increased by approximately 1.5 percent from the C608 throat area, to approximately 4.8 in^2. Additionally, the inlet lip radius was increased for improved low speed performance. Several other design elements from the C611 configuration were incorporated into the 2019 model, including:

- updated canards;
- updated vortex generators (positioned aft of the cockpit canopy) that were 50 percent taller than the "C608 Baseline" vortex generators tested during the 2017 Inlet Performance Test (Ref. 1);
- updated forward-vision camera fairing (the shape of the X–59 near the cockpit precludes the use of a standard cockpit canopy);
- longer nose (3.5 in. at 9.5 percent-scale);
- solid, non-flowing Environmental Control System (ECS) bumps on upper surface of wings.

The HSIDT model had several parts that could be substituted in order to assess the impact of recent design changes. These included:

- original short nose;
- flat panels to eliminate ECS bumps;
- alternate fuselage-mounted vortex generators that were twice the height as the standard HSIDT vortex generators.

Figure 3 shows the baseline ECS bump inserts and the ECS blank inserts. Likewise, Figure 4 shows the baseline fuselage-mounted vortex generators and the alternate fuselage-mounted vortex generators. The original short nose configuration was not tested during the HSIDT.
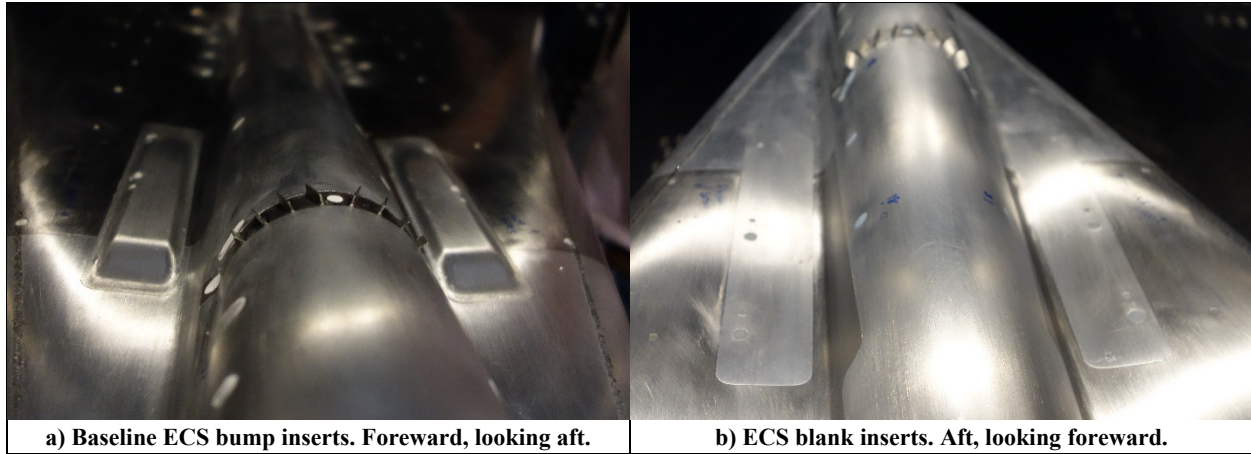
| a) Baseline ECS bump inserts. Foreward, looking aft. | b) ECS blank inserts. Aft, looking forward. |

Figure 3.—Comparison of baseline ECS bumps inserts and ECS blank inserts.

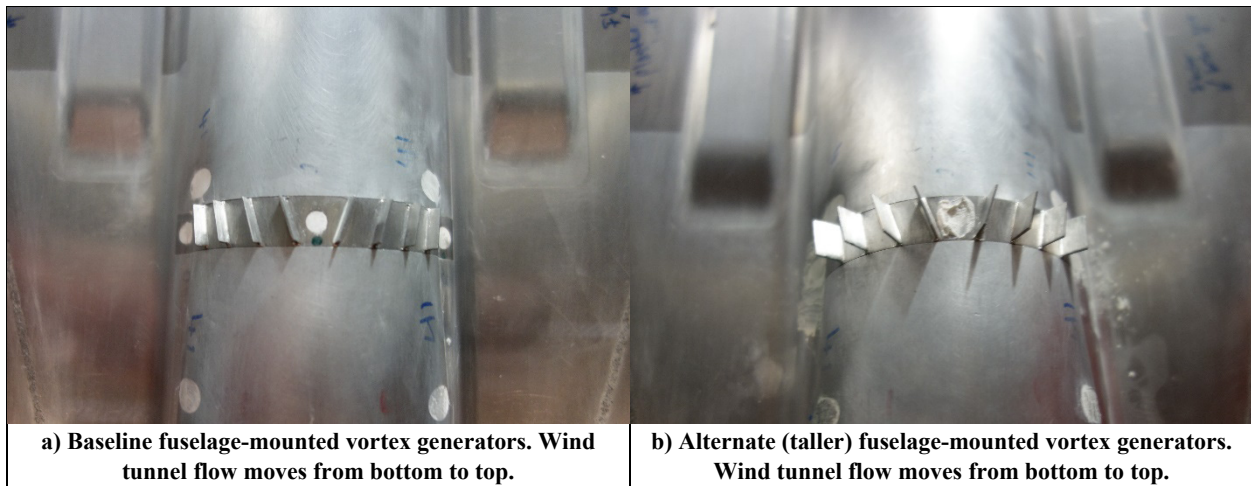| a) Baseline fuselage-mounted vortex generators. Wind tunnel flow moves from bottom to top. | b) Alternate (taller) fuselage-mounted vortex generators. Wind tunnel flow moves from bottom to top. |

Figure 4.—Comparison of baseline and alternate fuselage-mounted vortex generators.

TABLE 1.—ATTITUDE LIMITS OF QueSST MODEL IN THE NASA GLENN RESEARCH CENTER
8- BY 6-FOOT SUPERSONIC WIND TUNNEL

Tunnel Mach number	Angle-of-attack range	Angle-of-sideslip range	Strut height range, in.
0.3 to 0.4	−4° to 14°	−10° to +9°	27.2 to 48.7
0.6 to 1.1	−2° to +8°	−2° to +2°	39.8 (fixed)
1.1 to 1.6	−2° to +5°	−2° to +2°	39.8 (fixed)

The HSIDT model could be positioned within the wind tunnel test section with respect to height, angle-of-attack (pitch, α), and angle-of-sideslip (yaw, β). Model height was adjusted using the height of the transonic strut. A double knuckle on the sting-controlled model pitch and yaw. The maximum ranges for angle-of-attack, angle-of-sideslip, and strut height are listed in Table 1 for different test section Mach number intervals. These ranges were set by aerodynamic loads and model size. Figure 5 shows the tested angles-of-attack and angles-of-side slip at each Mach number with the X–59 control law limits for each. The HSIDT angle-of-attack range and angle-of-sideslip range met or exceeded the control law soft limits of the X–59 flight vehicle at nearly all Mach numbers. Angles-of-attack and angles-of-sideslip that were beyond the ranges tested during the HSIDT but within the X–59 control law hard limits represent vehicle attitudes that flight test engineers will need to closely monitor inlet and engine instrumentation during the X–59 flight tests.

a) Angle-of-attack test points and control law limits.   b) Angle-of-sideslip test points and control law limits.
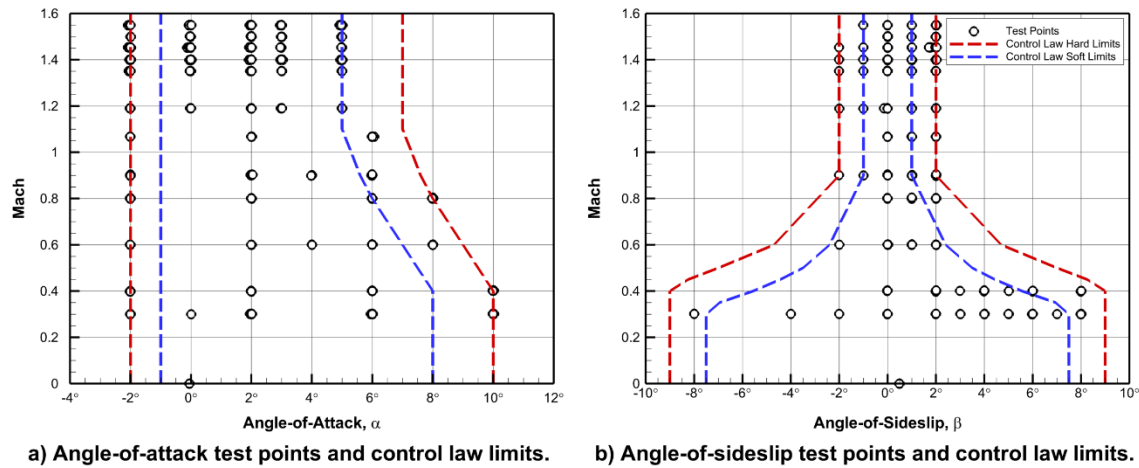
Figure 5.—HSIDT test point angles-of-attack and angles-of-sideslip with X–59 control law limits.
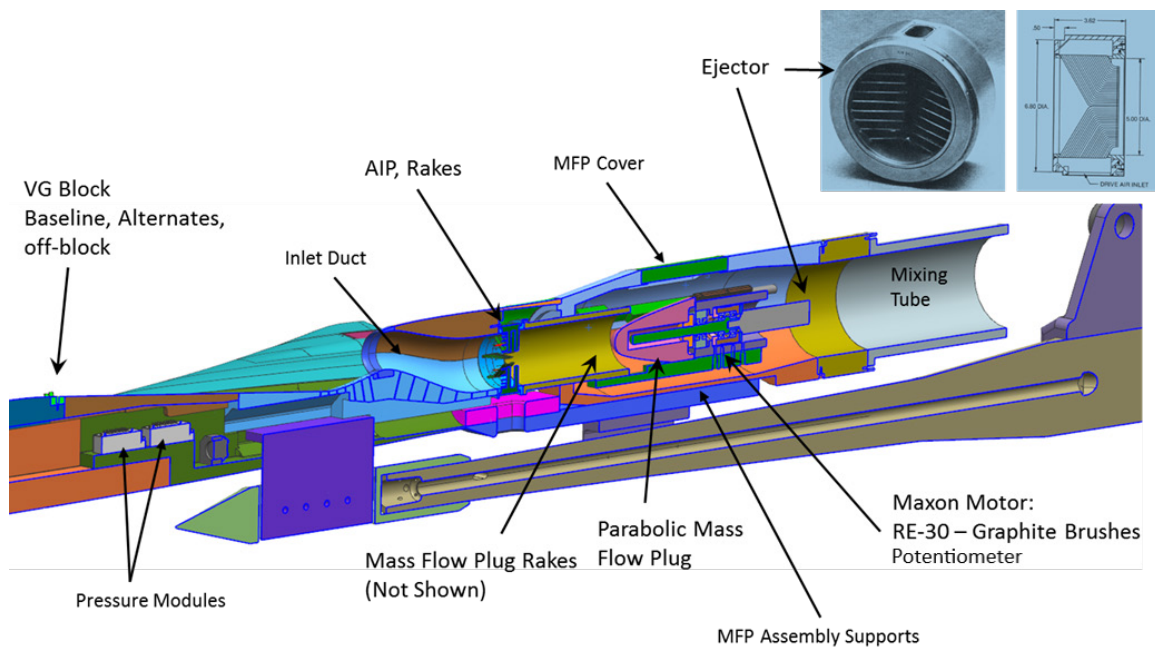

Figure 6.—Cut-away image of the HSIDT model inlet flow path, with key parts labeled.

2.2.2 Mass Flow Plug

Inlet mass flow rate was controlled using a calibrated mass flow plug mounted downstream of the Aerodynamic Interface Plane (AIP). Figure 6 shows a cut-away image of the inlet flow path, with the inlet duct, AIP, and mass flow plug labeled. A potentiometer was used to determine mass flow plug position. The mass flow plug's range of travel was increased for the HSIDT, from approximately 2.8 in. of travel to approximately 4.05 in. of travel. The increased range allowed the mass flow plug to move from nearly closed to fully open and gave the inlet the widest range of possible air flows.

An ejector (pictured in Figure 6) was installed downstream of the mass flow plug to help maintain choked flow. During testing at supersonic test section Mach numbers, the mass flow plug was choked without operating the ejector. At subsonic test section Mach numbers, the ejector was required to maintain choked flow across the mass flow plug, especially at low inlet mass flows. Despite the ejector operating, there were some conditions at the lowest test section Mach numbers and the lowest inlet mass flows in which the flow across the mass flow plug remained unchoked.

Following the 2017 Inlet Performance Test, the mass flow plug was calibrated to provide an equation for corrected mass flow rate as a function of plug position and pressure ratio across the plug. The calibration accounted for choked and unchoked flow. The HSIDT used that mass flow plug calibration, even though the calibration assumed a reduced range of mass flow plug travel. Following the HSIDT, the mass flow plug was recalibrated. With the extended travel, the 2019 mass flow plug calibration agreed with the 2017 mass flow plug calibration and no post-test recalculations were performed.

2.2.3 Instrumentation

The primary piece or focal point of instrumentation was the AIP rake. A photo of the uninstalled AIP assembly is pictured in Figure 7. The AIP rake for the 2019 HSIDT model was located at the scaled engine face plane and the inflow diameter of the AIP duct was 2.907 in. The AIP rake consisted of eight rakes with five steady-state pitot pressure probes and five high-response total pressure probes, located in a side-by-side (or "shotgun") arrangement. The high-response probe tubes were significantly larger in diameter than the steady-state pitot probe tubes (0.090 vs. 0.047 in.). The 2017 Inlet Performance Test used 0.060-in.-diameter steady-state pitot pressure probe tubes. The HSIDT used smaller pitot pressure probe tubes to reduce blockage at the AIP. The 40 pairs of probes were arranged in an equal-area configuration, based on the SAE ARP-1420 standard (Ref. 6).

The model included four high-response inlet static pressure probes located approximately 1.2 in. upstream of the AIP, on the upper surface of the inlet duct. The approximate locations of two of these probes can be seen in Figure 8. These high-response inlet static pressure probes were used to correlate inlet planar wave (commonly referred to inlet buzz) with the AIP high-response probes (the primary inlet planar wave detection instrumentation). The X–59 flight vehicle will be only instrumented with four high-response inlet static pressure probes upstream of the engine face, in a similar location as the HSIDT model, to detect inlet planar wave.
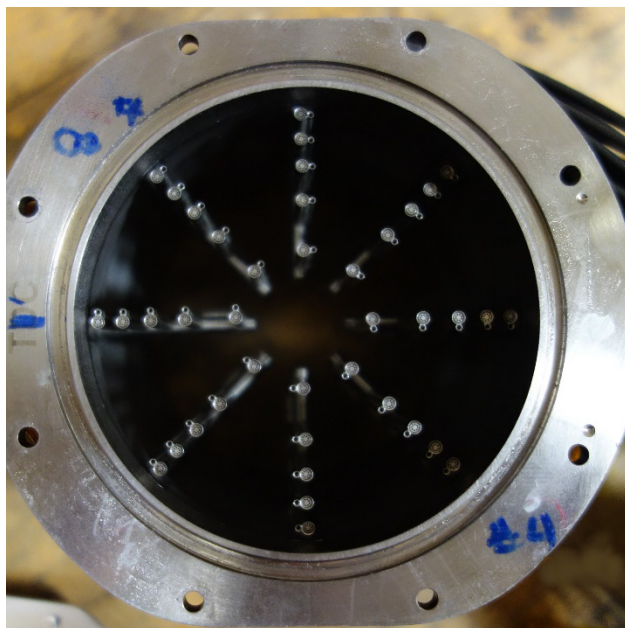

Figure 7.—Photo of uninstalled Aerodynamic Interface Plane (AIP) rake assembly. Smaller tubes are steady-state pitot probes; larger tubes contain high-response probes.
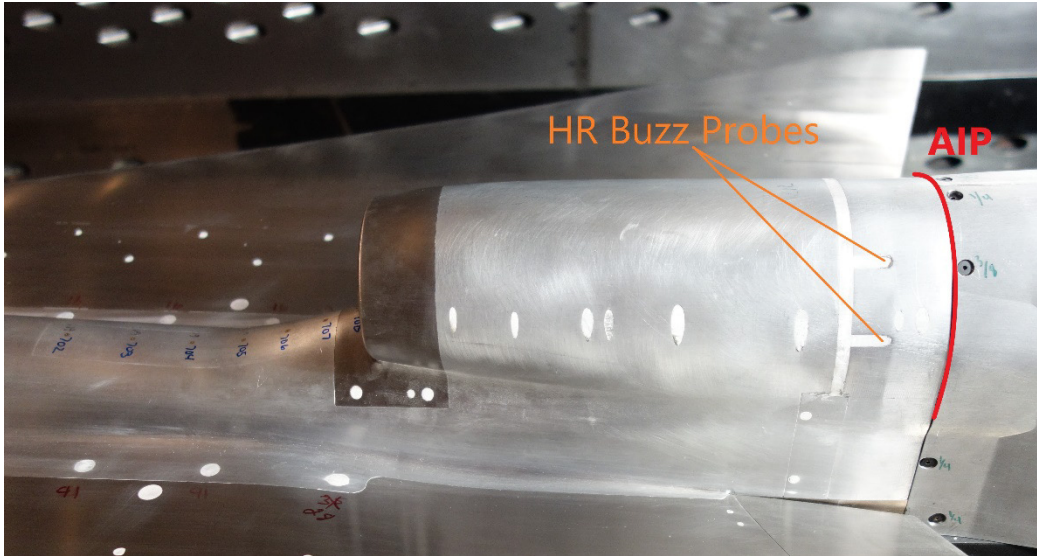
Figure 8.—Photo of left side of inlet nacelle. Labels show approximate locations of two (of four) high-response inlet static pressure probes, flush-mounted to the inlet duct, used for detecting inlet planar wave (inlet buzz) near the Aerodynamic Interface Plane (AIP). All instrumentation is internal.
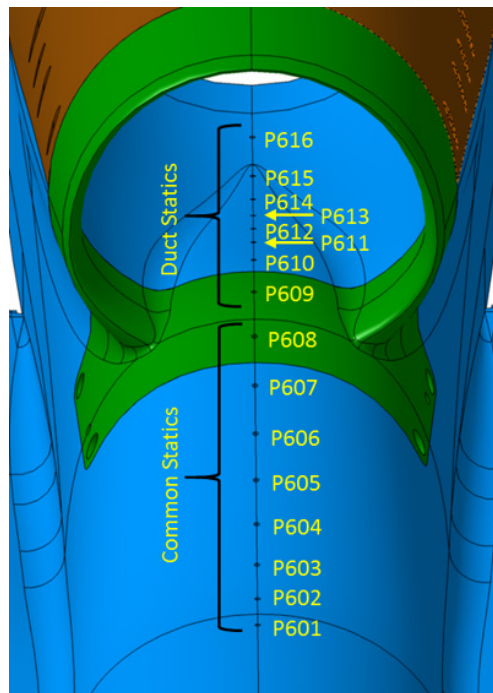

Figure 9.—Computer model showing the location of steady-state static pressure taps along the bump and inlet centerline.

Lastly, there were 16 steady-state static pressure probes located along the centerline of the model, spanning from upstream of the inlet bump to just upstream of the AIP (see Figure 9).

Steady-state total and static pressure measurements were scanned at a rate of 12.5 Hz and averaged over 3 s for each reading. High-response total and static pressure measurements were scanned at a rate of 20,000 Hz and sampled for three seconds, for a total of 60,000 scans per reading. The high-response data was low-pass filtered using a 10-sample moving average.

2.2.4 Pitot Pressure Probe Accuracy

As shown by Arend and Saunders (Ref. 7), the "Prati" probe configuration of the steady-state and high-response pitot pressure probe is more accurate than and preferred over the side-by-side arrangement used for the HSIDT. The side-by-side arrangement was selected for the HSIDT because its smaller cross-sectional area created less blockage at the AIP that the Prati probe configuration. Using the figures in Reference 7 and results from unpublished post-test computational fluid dynamics (CFD) simulations, it was possible to determine the accuracy of the steady-state and high-response pitot pressure probes. CFD simulations completed for the Mach = 1.45 tunnel conditions with an inlet mass flow ratio representative of the military power airflow showed the average Mach number at the inlet AIP to be approximately 0.43. Additionally, the CFD simulations showed that the swirl flow angularity ranged from –4° to +5° and that radial flow angularity ranged from –9° to +5°. Arend and Saunders show the measured reduction in total pressure for the steady-state and high-response pitot pressure probes in a side-by-side configuration across a range of pitch (corresponding to swirl angle for the HSIDT) and yaw (corresponding to radial angle for the HSIDT) at Mach = 0.3 and 0.6 in Figure 4 to Figure 7. The data looks linear in the range of the Mach, pitch angles, and yaw angles observed in the post-test CFD simulations of the HSIDT. Interpolating the data presented in Reference 7, the steady-state pitot pressure probes would be expected to read 0.3 to 0.9 percent below the actual total pressure. The high-response pitot pressure probes would be expected to read at the actual total pressure.

2.3 Test Procedures

Data was collected for inlet mass flow plug sweeps for specific tunnel Mach number, angle-of-attack, and angle-of-sideslip. With the model at zero angle-of-attack, zero angle-of-sideslip, and mass flow plug fully retracted (open), the 8x6 SWT was set for a specific calibrated Mach number. Upon reaching the specified tunnel Mach number, the model's angle-of-sideslip was set. Next, the model's angle-of-attack was set. At larger angle-of-attack and angle-of-sideslip attitudes, it was usually required to adjust the balance chamber pressure to return the test section to the desired calibrated Mach number. After the test section Mach number had settled, the mass flow plug was moved forward to the first position. The flow was allowed to settle for a few seconds before a steady-state reading and a high-response data scan were recorded. Following each three-second data recording, the mass flow plug was moved forward to the next position. The flow was allowed to settle for a few seconds and a new data recording was taken. In this manner, the inlet mass flow was reduced with subsequent data recordings. After completing the mass flow plug sweep, the mass flow plug was retracted to the fully open position and the model was adjusted for the next angle-of-attack and angle-of-sideslip position.

If the inlet encountered severe inlet planar wave conditions—that is, if levels of SUM40 (to be defined later) were beyond the limit set by the engine manufacturer—the mass flow plug was retracted until the inlet was no longer experiencing planar wave. One or more intermediate data recordings were taken between the last mass flow plug position free of inlet planar wave and the mass flow plug position at which the inlet planar wave was encountered.

2.4 Relevance of Test Scale

The X–59 propulsion model used in the HSIDT was 9.5 percent-scale, representing the largest full vehicle model that has been tested in the 8x6 SWT (Ref. 1). The Reynolds number for the HSIDT model at Mach = 1.45 was approximately 1.28 million, using the engine face (i.e., AIP) diameter as the reference length, and 5.6 million, using the distance from the beginning of the inlet bump to the AIP as the reference length. These Reynolds numbers are about 34 percent of the flight-scale Reynolds number.

(The HSIDT Reynolds number-scale, 34 percent, is significantly larger than the model-scale of 9.5 percent due to the 8x6 SWT being an atmospheric wind tunnel, the density of air being that for 780 ft elevation, rather than for the 53,000 ft flight vehicle cruise altitude.) Norby (Ref. 8) conducted inlet testing with model scales of 6 and 12 percent and recommended engine face diameter-based Reynolds numbers of 1 million to produce data independent of Reynolds number effects. SAE AIR-5687-2011 (Ref. 9) suggested that model-scale inlets with inlet ramp distance-based Reynolds number greater than 2 million are required to obtain distortion results independent of Reynolds number effects. The HSIDT model and test facility was consistent with both sets of recommendations and should be expected to produce inlet distortion and performance data independent of Reynolds number effects.

3.0 Results

The HSIDT was preceded by the QueSST Inlet Performance Test (Ref. 1). Steady-state pre-test CFD simulations were completed to assess changes in the HSIDT test model geometry made since the Inlet Performance Test. The results of the pre-test CFD were discussed in a limited-availability NASA Technical Memorandum (Ref. 10), and will not be discussed here. The Inlet Performance Test and pre-test CFD simulations gave indication of the steady-state inlet performance expected of the present test, but the HSIDT represented the first high-response data collected on the X–59's unique top-mounted, diverterless bump inlet.

3.1 Definition of Analysis Parameters and Conventions

Data is grouped into three speed regimes: subsonic, Mach 0.3 to 0.4; "transonic," Mach 0.6 to 1.19; and supersonic, Mach 1.35 to 1.55. When data was available, a fourth speed regime is included: Mach 0, no tunnel flow with the ejector operating. The supersonic and transonic data is plotted for a nominal aircraft attitude ($\alpha = 2°$, $\beta = 0°$); the subsonic data is plotted for a larger range of aircraft attitudes ($\alpha = 2°$, 6°, and 10°, $\beta = 0°$), including larger angles-of-attack that would be expected during take-off and landing. Expanded ranges of angle-of-attack and angle-of-sideslip will be presented later when looking at the sensitivities to aircraft attitude parameters.

Mass flow is reported using the 2017 unchoked mass flow plug calibration. The mass flow plug calibration completed in 2019 (following the HSIDT) verified the 2017 calibration and no changes were made. The inlet mass flow is non-dimensionalized using the inlet throat area (approximately 4.8 in^2), rather than the inlet capture area. The capture area is difficult to define on a bump inlet, and so the throat area is used as the reference. A result of this decision is that the mass flow ratio can be greater than one.

Distortion is presented as the GE radial distortion parameter, IDRMAX, and the GE circumferential distortion parameter, IDCMAX. IDRMAX is equal to the SAE ARP 1420 (Ref. 6) radial distortion parameter, DPRP, while IDCMAX is similar to the SAE ARP 1420 circumferential distortion parameter, DPCP, with a modified extent factor. Distortion parameters are presented using the AIP steady-state and the high-response total pressure probes. During data processing, the mean of each high-response total pressure reading was re-centered using the adjacent steady-state pitot pressure probe. When high-response total pressure probes were found to be damaged or not operating properly, substitutions were made according to SAE ARP 1420.

Inlet planar waves (or inlet buzz), as defined by SAE AIR-5866 (Ref. 11), are "one-dimensional [in-phase] total pressure fluctuations at the compressor face." Inlet planar waves may reduce engine stability margin and damage the engine. During the HSIDT, inlet planar waves were indicated by the AIP high-response total pressure probes using a root-mean-square calculation, SUM40:

$$\text{SUM40} = \left(\sqrt{\sum_{i=1}^{\text{NSCAN}} \left[\left((p_{t2}/p_{t0})_{dynamic} \right)_i - \left((p_{t2}/p_{t0})_{mean} \right) \right]^2 / \text{NSCAN}} \right) / \left((p_{t2}/p_{t0})_{mean} \right) \quad (1)$$

In Equation (1), the dynamic total pressure recovery, $(p_{t2}/p_{t0})_{dynamic}$, is taken at each scan, whereas the mean total pressure recovery, $(p_{t2}/p_{t0})_{mean}$, was the mean of the dynamic total pressure recovery over the 60,000 scans. (It should be noted that this report uses the term "average" for spatial averages, and the term "mean" for temporal averages.) As with the distortion parameters, substitutions were made using guidance from SAE ARP 1420 when a high-response probe was found to be damaged or improperly operating.

In a similar manner, SUM4 was computed for the four high-response inlet static pressure probes located on the upper surface of the inlet duct upstream of the AIP:

$$\text{SUM4} = \left(\sqrt{\sum_{i=1}^{NSCAN} \left[\left((p_{s2})_{dynamic} \right)_i - \left((p_{s2})_{mean} \right) \right]^2 / \text{NSCAN}} \right) / \left((p_{s2})_{mean} \right) \quad (2)$$

In Equation (2), p_{s2} is the average of the four high-response static pressure probes on the upper surface of the inlet duct. (The freestream total pressure term, p_{t0}, was neglected in Equation (2) to keep the calculation of SUM4 as simple as possible for the eventual use during flight testing of the X–59 and also because the term divides out.)

Steady-state inlet total pressure recovery is presented using the AIP steady-state pitot pressure probes. Inlet total pressure recovery computed using the mean of the AIP high-response total pressure probes will be denoted as such.

Some frequency analysis was performed to determine the frequencies of inlet planar wave. The frequency analysis was completed by way of plotting the power spectral density (PSD), defined by:

$$\text{PSD} = 10 \times \log_{10} \left[2 \times \left(\frac{1}{Fs \times \text{NSCAN}} \right) \times \left| \text{FFT} \left((p_{t2})_{dynamic} - (p_{t2})_{mean} \right) \right|^2 \right] \quad (3)$$

In Equation (3), Fs is the high-response sampling frequency, 20,000 Hz, and NSCAN is the number of samples, 60,000. A fast Fourier transform (FFT) is performed on the difference between the dynamic area-average of the AIP total pressures, $(p_{t2})_{dynamic}$, and the mean area-average of the AIP total pressures, $(p_{t2})_{mean}$. Power spectral density is plotted with respect to frequency and the resulting plot shows what, if any, resonant frequencies are present in the inlet flow.

The engine manufacturer provided limits for circumferential distortion, radial distortion, and SUM40. While these limits were used in the analyses presented here to assess the inlet performance, the limits will not be presented in this report due to their sensitive nature.

3.2 Inlet Total Pressure Recovery

While the focus of the HSIDT was to assess the X–59 inlet/engine face dynamic effects—i.e., inlet distortion and inlet planar wave—inlet total pressure recovery was also examined. Figure 10 shows the inlet total pressure recovery, p_{t2}/p_{t0}, as a function of inlet mass flow ratio at subsonic, transonic, and supersonic Mach numbers. It is important to note that the X–59 inlet will not be operated at supercritical airflows (where inlet total pressure recovery drops sharply as the inlet mass flow ratio increases), and thus

the HSIDT did not test supercritical inlet mass flow ratios at all Mach numbers. Figure 10(a) shows that, for subsonic tunnel Mach numbers, total pressure recovery decreases by 6 to 7 percent as the inlet mass flow ratio increases above 1. Additionally, total pressure recovery decreases by 1 to 2 percent at the "knee" of the curve as angle-of-attack increases from 2° to 10°. Figure 10(b) and (c) show that the total pressure recovery continues to decrease as tunnel Mach number increases. In Figure 10(c), the total pressure recovery is likely greater than normal-shock recovery for much of the mass flow ratio range due to the bump adding external compression to the inlet flow. At the "cruise" Mach number (Mach = 1.45) the inlet total pressure recovery ranges from 0.92 to nearly 0.99, depending on inlet mass flow ratio. As described in Section 2.0, changes were made to the wind tunnel model geometry between the 2017 Inlet Performance Test and the 2019 High Speed Inlet Distortion Test, reflecting updates to the X–59 flight vehicle geometry. Comparing the inlet total pressure recovery with the result presented by Castner, et al. for the Inlet Performance Test (Ref. 1), the HSIDT inlet performs similarly to the results from the earlier test.
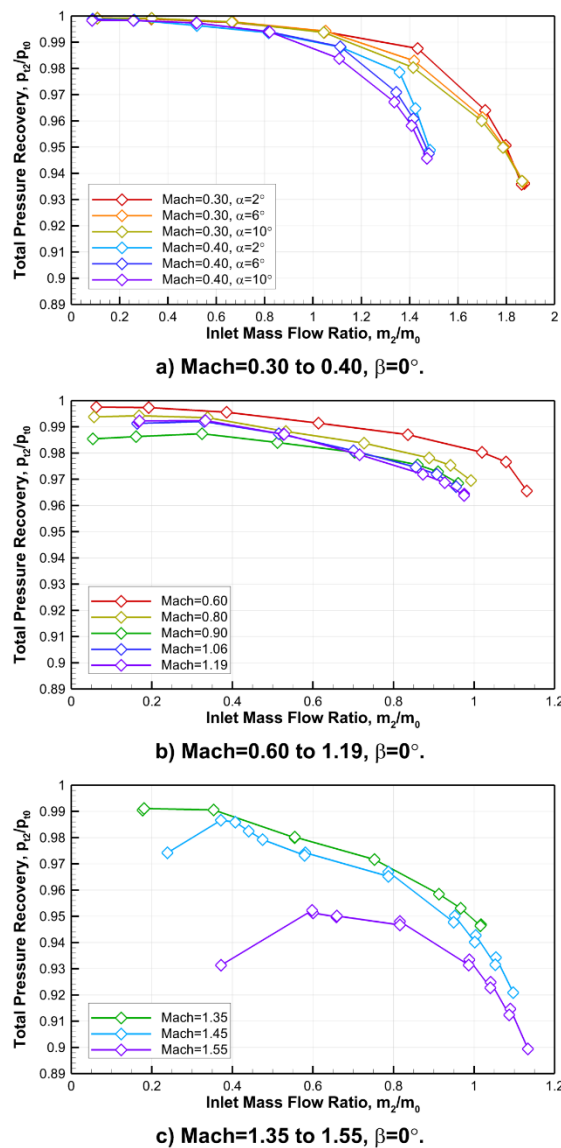

a) Mach=0.30 to 0.40, β=0°.

b) Mach=0.60 to 1.19, β=0°.

c) Mach=1.35 to 1.55, β=0°.

Figure 10.—Inlet total pressure recovery. Baseline vortex generators, ECS bumps, and nose.

3.3 Dynamic Distortion Analysis

The primary objective of the X–59 HSIDT was to evaluate the compatibility of the inlet and engine based on the dynamic effects presented by the inlet to the engine face. The high-response inlet distortion can be plotted in scatter plots, showing the instantaneous distortion parameters at each scan (high-response sample) during a reading (steady-state sampling at specific Mach, angle-of-attack, angle-of-sideslip, mass flow plug position). Examples of typical distortion scatter plots are shown in Figure 11. Figure 11(a) shows a typical compact scatter plot. Figure 11(b) shows a wide scatter plot, in which the instantaneous distortion has a broad range. Figure 11(c) and (d) show scatter plots for the inlet experiencing planar waves.

The steady-state and maximum instantaneous values of the high-response distortion are plotted in Figure 12. Symbols of the same style and color represent data acquired within a mass flow sweep at a specific Mach, angle-of-attack, and angle-of-sideslip (see Figure 10). Generally, distortion increases as inlet mass flow increases. It should be noted that the plotted values of the high-response IDCMAX and IDRMAX (labeled "HR Max") are maximum values for each distortion parameter, and they did not necessarily occur at the same time. At zero flow, shown in Figure 12(a), the maximum values of high-response circumferential and radial distortion are significantly greater than steady-state values of each—about 11 percent greater for circumferential distortion and about 8 percent greater for radial distortion. The test points with the highest distortion represent inlet mass flow ratios greater than the what the inlet

a) Small cloud. HR reading 78:
Mach=1.55, α=2°, β=0°, m_2/m_0=0.922.

b) Large cloud. HR reading 282:
Mach=1.55, α=-2°, β=2°, m_2/m_0=0.931.

c) Inlet planar wave. HR reading 445:
Mach=1.45, α=-2°, β=0°, m_2/m_0=0.062.

d) Inlet planar wave with high distortion. HR reading 284:
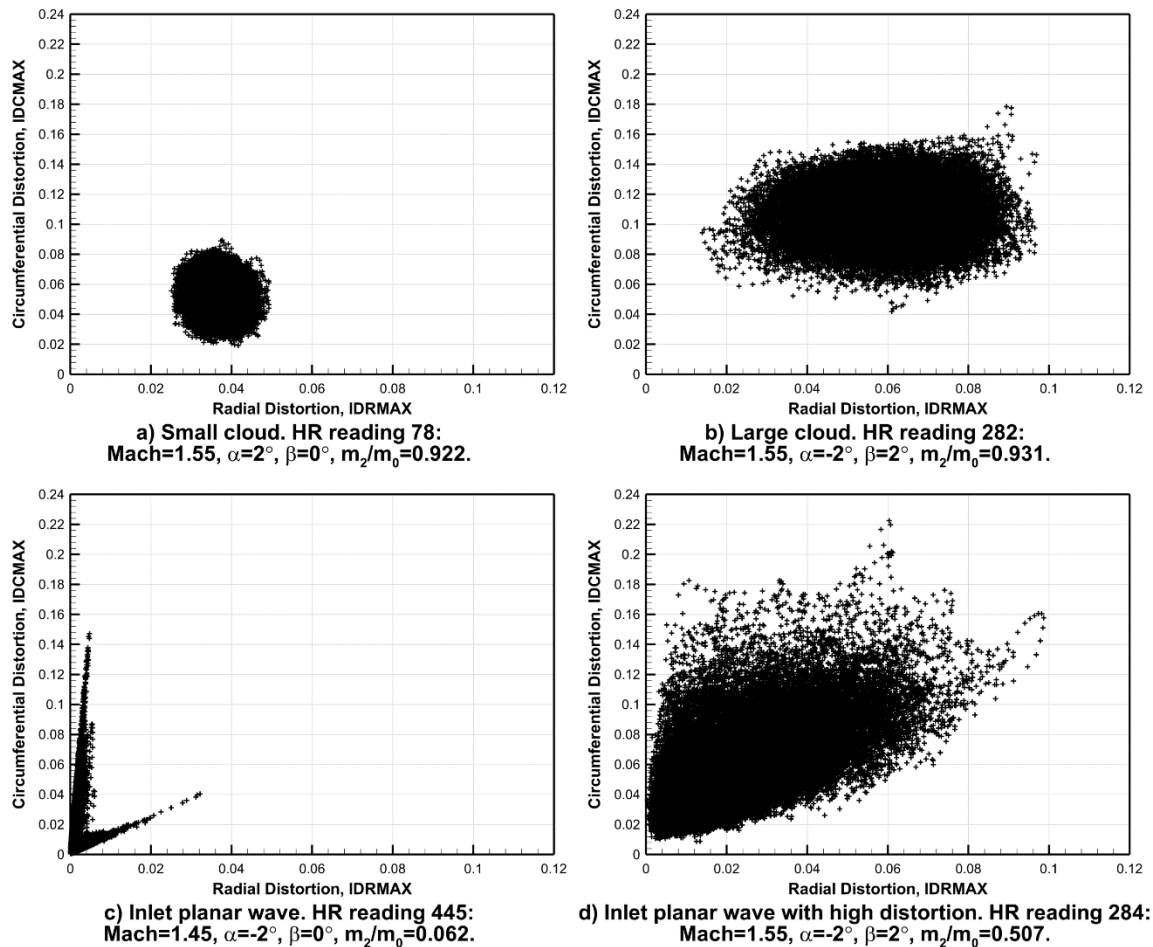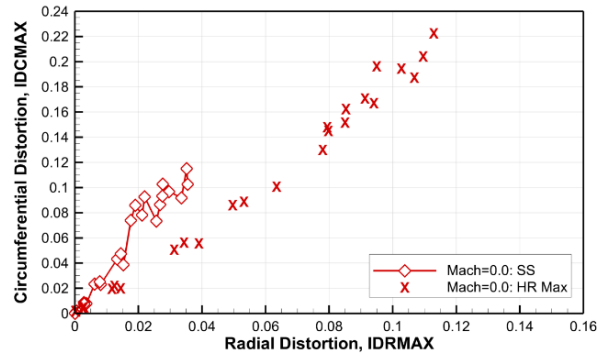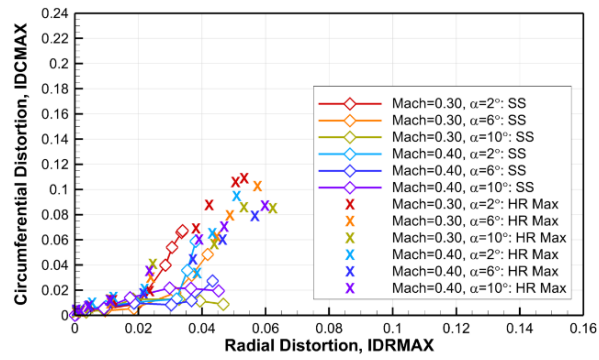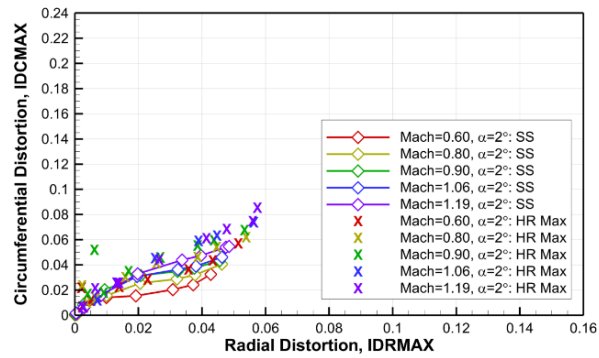Mach=1.55, α=-2°, β=2°, m_2/m_0=0.507.

Figure 11.—Samples of high-response inlet distortion scatter plots.

a) Mach=0.0.
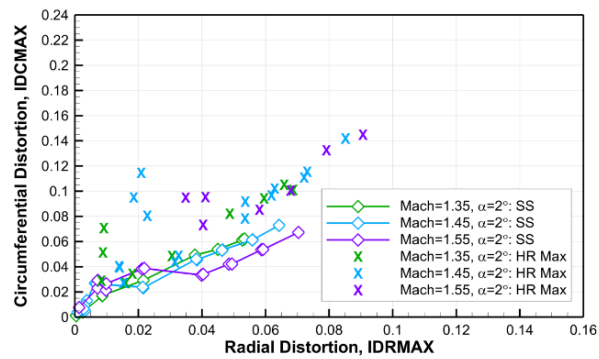

b) Mach=0.30 to 0.40, β=0°.

c) Mach=0.60 to 1.19, β=0°.

d) Mach=1.35 to 1.55, β=0°.

Figure 12.—Steady-state and maximum levels of dynamic distortion. Baseline vortex generators, ECS bumps, and nose.

and engine would actually see on the flight vehicle. At subsonic Mach numbers, shown in Figure 12(b), the differences between maximum high-response distortion and the steady-state distortion are smaller than at Mach = 0, but they are still significant. The high-response distortion is more closely aligned with the steady-state values for $\alpha = 2°$, while the high-response values are up to 3 percent greater than the steady-state radial distortion and 8 percent greater than steady-state circumferential distortion. At the transonic Mach numbers, in Figure 12(c), the maximum high-response distortion was in much closer alignment with the steady-state distortion, generally within 1 percent for radial distortion and 2 percent for circumferential distortion. For the supersonic tunnel Mach numbers, in Figure 12(d), it is observed that the maximum values of the high-response distortion are significantly greater than the steady-state distortion: the high-response radial distortion is up to 2 percent greater than the steady-state value; and the high-response circumferential distortion is up to 12 percent greater than the steady-state value.

Figure 13 shows the ratio of maximum high-response values to steady-state values for IDCMAX and IDRMAX across the inlet air flow sweeps for subsonic, transonic, and supersonic wind tunnel Mach numbers. A semi-log scale is used to show the large ratios at low inlet air flows, but it is important to

a) Ratio of high response to steady-state circumferential distortion, Mach=0.30 to 0.40, $\beta=0°$.

b) Ratio of high response to steady-state radial distortion, Mach=0.30 to 0.40, $\beta=0°$.

c) Ratio of high response to steady-state circumferential distortion, Mach=0.60 to 1.19, $\beta=0°$.

d) Ratio of high response to steady-state radial distortion, Mach=0.60 to 1.19, $\beta=0°$.

e) Ratio of high response to steady-state circumferential distortion, Mach=1.35 to 1.55, $\beta=0°$.

f) Ratio of high response to steady-state radial distortion, Mach=1.35 to 1.55, $\beta=0°$.
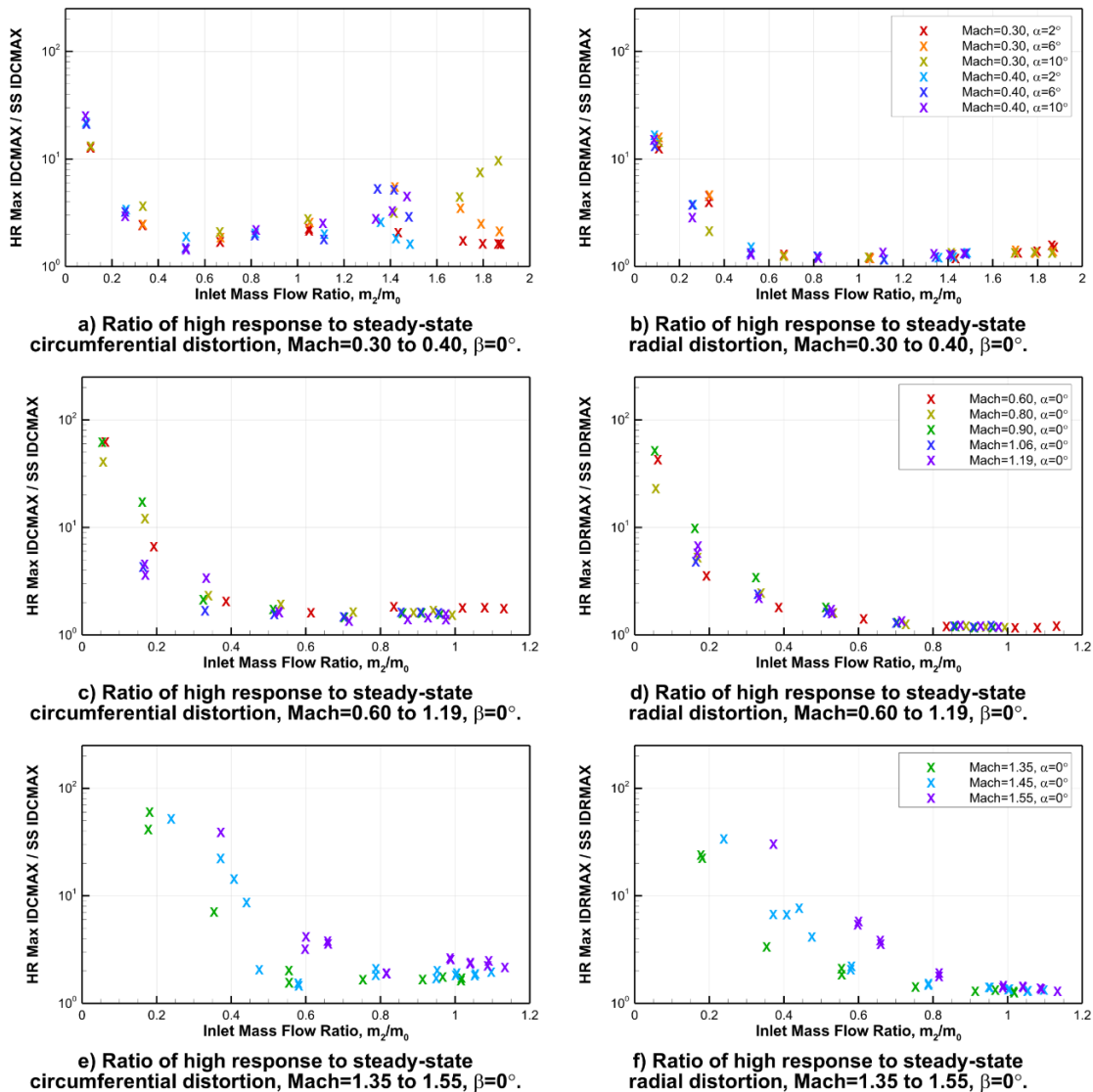
Figure 13.—The ratio of maximum high-response distortion to steady-state distortion as a function of inlet air flow. Baseline vortex generators, ECS bumps, and nose.

remember that the steady-state radial and circumferential distortion levels are small for low air flows. Figure 13(a) and (b) show that the ratio of maximum high-response distortion to steady-state distortion for subsonic Mach numbers, and inlet mass flow ratios greater than 0.4, is between 1 and 1.6 for radial distortion. The same ratio for circumferential distortion is much more scattered for inlet mass flow ratios greater than 0.4. Generally, as angle of attack increases, the ratio of maximum high-response circumferential distortion to steady-state circumferential distortion also increases, though this is not always the case (see Figure 13(a) for m_2/m_0 = 1.1 to 1.42 for Mach = 0.4). Like the transonic and supersonic Mach numbers, the ratio of high-response distortion to steady-state distortion increases as the inlet mass flow ratio decreases below 0.4. As shown in Figure 13(c) and (d), the ratio of maximum high-response distortion to steady-state distortion is below 2 for inlet mass flow ratios greater than 0.4, for both circumferential and radial distortion. It is only at the smallest inlet air flows that the ratio of maximum high-response distortion to steady-state distortion increases to 62 (circumferential) and 51 (radial). For supersonic Mach numbers, Figure 13(e) and (f) show that the ratio of maximum high-response distortion to steady-state distortion, for mass flow ratios (m_2/m_0) greater than 0.8, was less than 3 for circumferential distortion and less than 2 for radial distortion. The maximum values of the ratio occurred at Mach 1.55 for circumferential and radial distortion. As the inlet mass flow ratio was reduced below 0.8, the ratio of the maximum high-response distortion to steady-state distortion increases, up to 60 for circumferential distortion (Mach 1.35) and 34 for radial distortion (Mach 1.45). This series of plots shows that, for the X–59 inlet, the steady-state values of circumferential and radial distortion are not a good approximation for the maximum high-response values of distortion.

Circumferential distortion (IDCMAX) and radial distortion (IDRMAX) are plotted as functions of angle-of-attack and angle-of-sideslip in Figure 14 and Figure 15, respectively, for subsonic, transonic, and supersonic tunnel Mach numbers at the inlet design airflow. Generally, steady-state and high-response circumferential distortion decreased as angle-of-attack increased. The one exception is observed in Figure 14(c): Mach = 0.4 and β = 0°, circumferential distortion increased as angle-of-attack increased. Steady-state and high-response radial distortion was rather insensitive to angle-of-attack for subsonic and transonic tunnel Mach numbers. At supersonic tunnel Mach numbers (Figure 14(h)), there was some variation in high-response radial distortion, with a maximum between α = 0° and 2° and minimum at α = 5°. The variation was less than 2 percent. The general behavior of circumferential and radial distortion is not easily characterized as angle-of-sideslip is varied. As observed in Figure 15(a) and (c), at subsonic Mach numbers, high-response circumferential distortion increased as angle-of-sideslip increased. Steady-state circumferential distortion also increased with angle-of-sideslip for most conditions at subsonic Mach numbers. At transonic Mach numbers, high-response and steady-state circumferential distortion decreased by up to 2 percent as angle-of-sideslip increased from 0° to 2° (Figure 15(e)). Figure 15(b), (d), and (f) show that, at subsonic and transonic Mach numbers, high-response and steady-state radial distortion was generally not very sensitive to angle-of-sideslip from 0° to 4°, but it did decrease by about 1 percent at the largest sideslip angles at Mach 0.3 and 0.4. At supersonic Mach numbers, shown in Figure 15(g) and (h), there was some reduction in circumferential and radial distortion at a sideslip angle of 1°. It is suspected that the inlet bump generates some distortion at zero sideslip—this was observed in steady-state CFD predictions—whereas a small sideslip angle provides the inlet with more uniform flow.
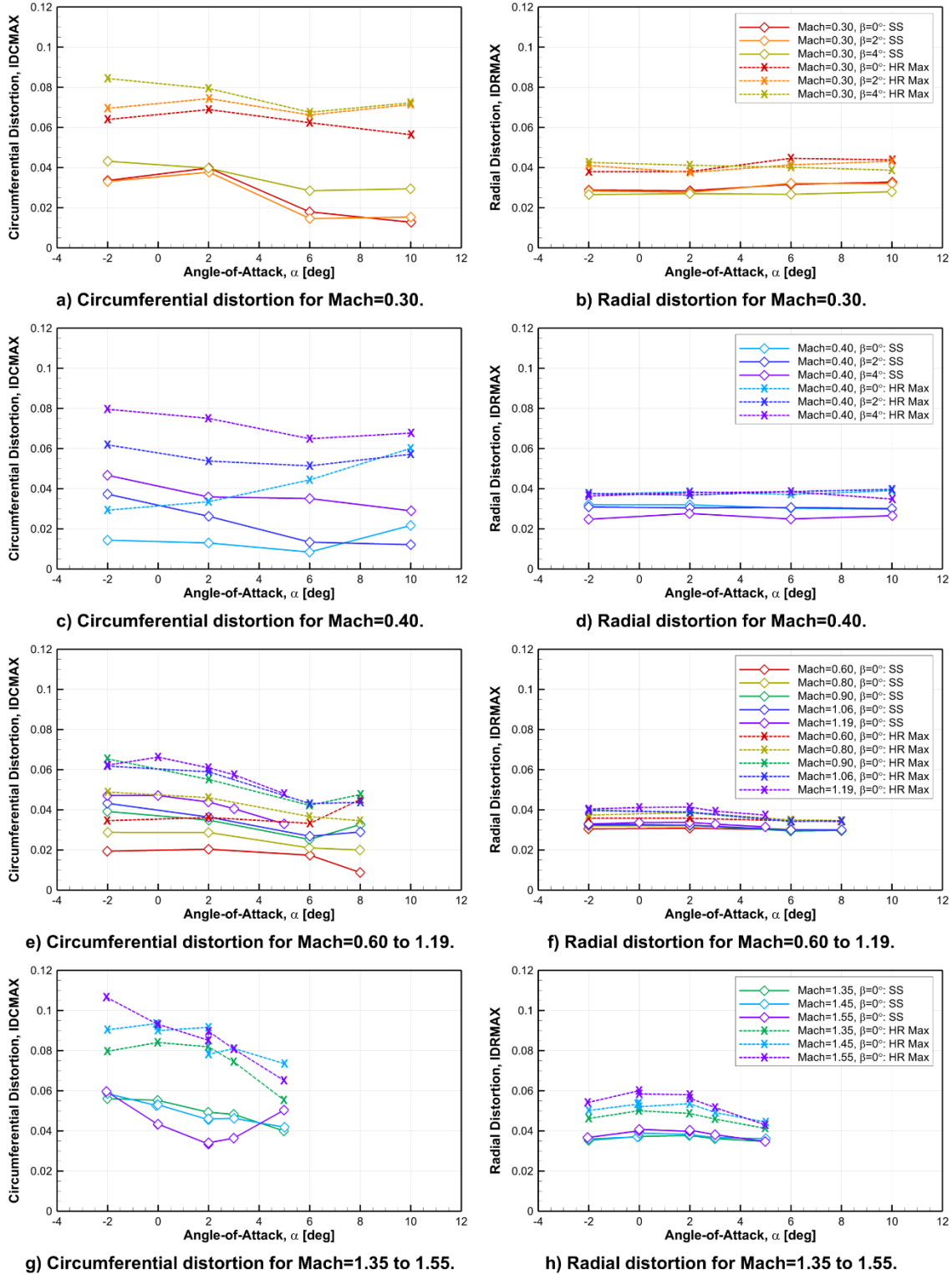
a) Circumferential distortion for Mach=0.30.

b) Radial distortion for Mach=0.30.

c) Circumferential distortion for Mach=0.40.

d) Radial distortion for Mach=0.40.

e) Circumferential distortion for Mach=0.60 to 1.19.

f) Radial distortion for Mach=0.60 to 1.19.

g) Circumferential distortion for Mach=1.35 to 1.55.

h) Radial distortion for Mach=1.35 to 1.55.

Figure 14.—Sensitivity of inlet distortion parameters to variations in angle-of-attack. Approximate maximum operating corrected inlet mass flow. Baseline vortex generators, ECS bumps, and nose.
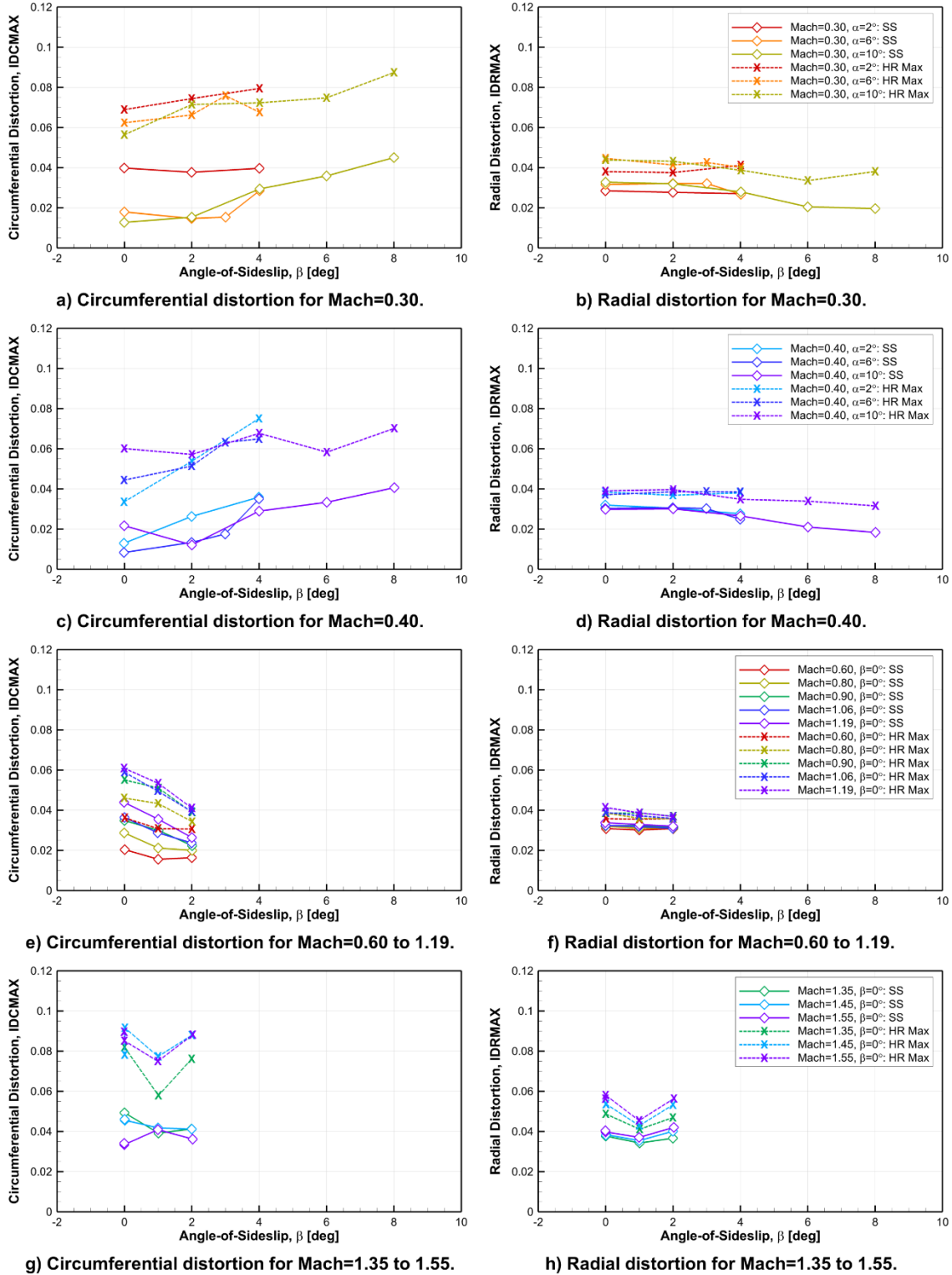
a) Circumferential distortion for Mach=0.30.

b) Radial distortion for Mach=0.30.

c) Circumferential distortion for Mach=0.40.

d) Radial distortion for Mach=0.40.

e) Circumferential distortion for Mach=0.60 to 1.19.

f) Radial distortion for Mach=0.60 to 1.19.

g) Circumferential distortion for Mach=1.35 to 1.55.

h) Radial distortion for Mach=1.35 to 1.55.

Figure 15.—Sensitivity of inlet distortion parameters to variations in angle-of-sideslip. Approximate maximum operating corrected inlet mass flow. Baseline vortex generators, ECS bumps, and nose.

3.4   SUM40

SUM40 was computed as an indicator of inlet planar wave. Figure 16 shows SUM40 with respect to the inlet mass flow ratio at subsonic, transonic, and supersonic tunnel Mach numbers. SUM40 is less than 0.25 percent at Mach 0.3 and 0.4 (Figure 16(a) and (b)) for all angles-of-attack and mass flow ratios. Values of SUM40 are similarly low (below 0.20 percent) at transonic tunnel Mach numbers (Figure 16(c)) for all but the lowest mass flow ratios. It is only for mass flow ratios below 0.2 that values of SUM40 increases substantially, up to 4 percent—significantly greater than the threshold indicating inlet planar wave. However, it is unlikely that the inlet would experience mass flows this low during actual flight, as these are well below minimum engine operating mass flows. Figure 16(d) shows that inlet planar wave becomes more of a concern as the vehicle Mach number increases, from 1.35 to 1.55. SUM40 increases sharply as the inlet mass flow ratio decreases below 0.36 at Mach = 1.35, 0.48 at Mach = 1.45, and 0.8 at Mach = 1.55. Due to the larger mass flow ratios at which the increase was observed, the HSIDT showed that inlet planar wave could be experienced at supersonic flight Mach numbers for engine airflows between idle and full military power. Airflow management will be required to avoid inlet planar wave that could damage the engine.

In Figure 17, PSD plots are shown for two supersonic test points from Figure 16(d) with SUM40 values indicating inlet planar wave. These data points are at nominal angle-of-attack and angle-of-sideslip ($\alpha = 2°$, $\beta = 0°$, respectively). The frequency axis is plotted from 2 to 2,000 Hz (corresponding with the low-pass data filter) using a semi-logarithmic scale. The energy in these PSD plots is broadly distributed across frequencies up to 200 Hz, at which point the energy magnitude falls off. Test points at off-nominal angle-of-attack and angle-of-sideslip at Mach = 1.45 and Mach = 1.55 were also examined: PSD plots from two off-nominal supersonic test points are shown in Figure 18. In each plot, a peak of energy is observed at approximately 173 Hz. SAE AIR5866 (Ref. 11) suggests that inlet planar wave frequency follows organ pipe theory and is inversely proportional to the scale factor. Therefore, the 173 Hz inlet planar wave frequency for the 9.5 percent-scale model would be about 16 Hz for the flight vehicle. It should be noted that the inlet mass flow ratio is very low for these points ($m_2/m_0 = 0.237$ and $m_2/m_0 = 0.194$). It is likely that these mass flows may be below the flight idle airflows and the inlet would not experience air flows this low during normal operation. Inlet planar wave was also observed through SUM40 and PSD plots at some subsonic tunnel Mach numbers. Figure 19 shows PSD plots for two test points at Mach 0.60 and 0.90. An energy peak is present at approximately 173 Hz. As with the test points shown in Figure 18, the inlet mass flow ratio is very low ($m_2/m_0 = 0.062$ and $m_2/m_0 = 0.057$) and it is unlikely that the inlet will see these air flows during normal operation.

3.5   SUM4 vs. SUM40

The X–59 flight vehicle will be instrumented with only four high-response static pressure sensors located upstream of the engine face to detect inlet planar wave. In addition to the 40 high-response total pressure probe array located at AIP, the HSIDT model was instrumented with four high-response static pressure probes located upstream of the AIP, in approximately the same location (9.5 percent-scale) as the static pressure probes on the flight vehicle. SUM4 was computed from these four high-response inlet static pressure probes, as shown in Equation (2), and compared to the values of SUM40 computed from the 40-probe AIP array. Figure 20 shows the difference between SUM40 and SUM4 versus inlet mass flow ratio at subsonic, transonic, and supersonic tunnel Mach numbers. SUM4 shows good agreement with SUM40 across most of the mass flow sweep for each tunnel Mach number. Looking back at Figure 16, SUM40 values were the largest at supersonic tunnel Mach numbers (Mach = 1.35 to 1.55) as inlet mass flow ratios decreased below 0.8. Figure 20(d) shows that the difference between SUM40 and SUM4 for $m_2/m_0<0.8$ is about ±0.03 percent for Mach = 1.35, up to 0.12 percent for Mach = 1.45, and up

to 0.08 percent for Mach = 1.55. Some of the larger SUM40-SUM4 differences are at inlet mass flow ratios below normal engine airflows. Furthermore, the differences in magnitude between SUM40 and SUM4 are one to two orders of magnitude less than the SUM40 threshold indicating inlet planar wave. Therefore, it is expected that SUM4 should be a good surrogate for SUM40 to detect inlet planar wave during the flight test.
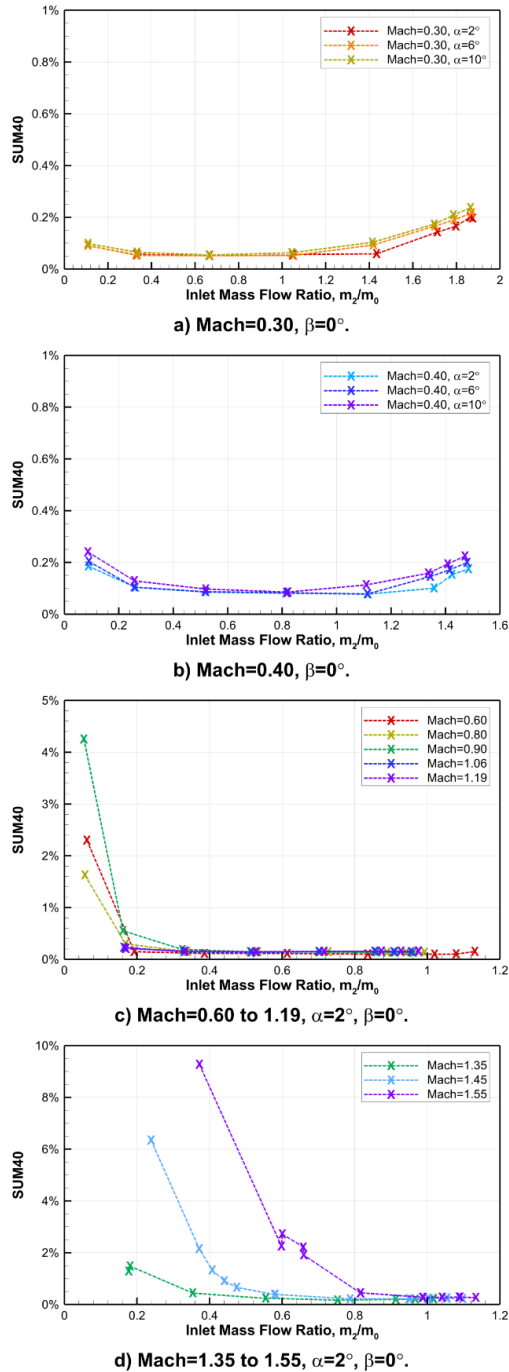

a) Mach=0.30, β=0°.

b) Mach=0.40, β=0°.

c) Mach=0.60 to 1.19, α=2°, β=0°.

d) Mach=1.35 to 1.55, α=2°, β=0°.

Figure 16.—Sensitivity of SUM40 to variations in inlet mass flow ratio. Baseline vortex generators, ECS bumps, and nose.

a) Mach=1.45, α=2.0°, β=0.0°, m_2/m_0=0.371.

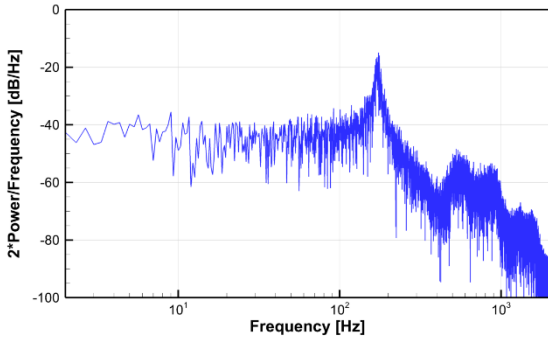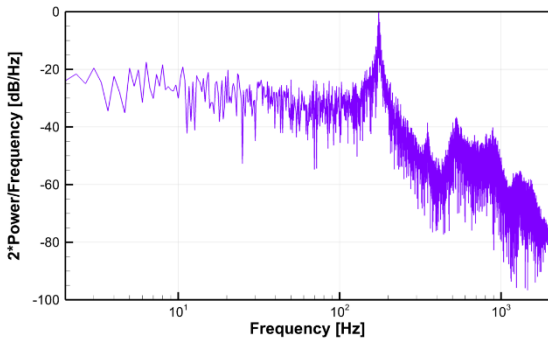b) Mach=1.55, α=2.0°, β=0.0°, m_2/m_0=0.598.
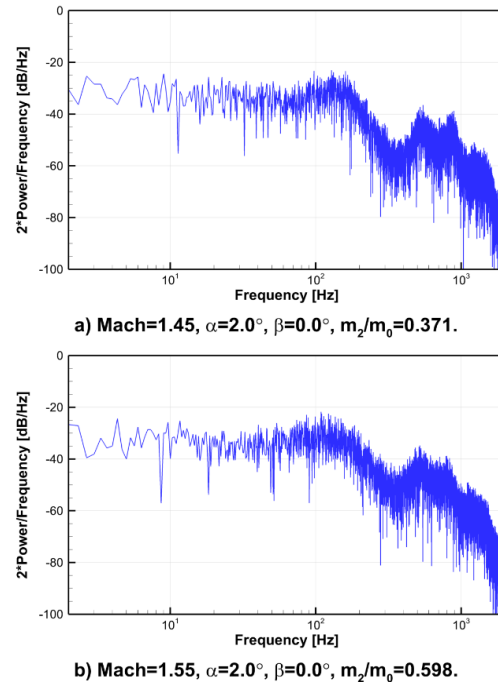
Figure 17.—Examples of power spectral density plots for Mach = 1.45 and Mach = 1.55 test points experiencing inlet planar wave, at nominal angle-of-attack and angle-of-sideslip. Baseline vortex generators, ECS bumps, and nose.
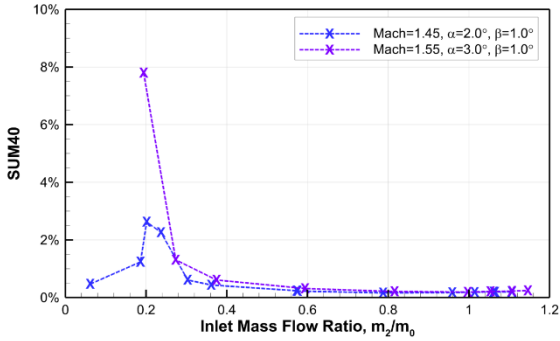
a) SUM40 for selected off-nominal configurations.

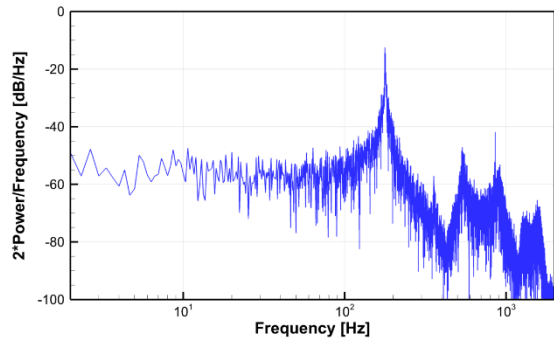b) Mach=1.45, α=2.0°, β=1.0°, m_2/m_0=0.237.

a) Mach=0.60, α=2.0°, β=1.0°, m_2/m_0=0.062.

c) Mach=1.55, α=3.0°, β=1.0°, m_2/m_0=0.194.

b) Mach=0.90, α=-2.0°, β=1.0°, m_2/m_0=0.057.

Figure 18.—Examples of power spectral density plots of Mach = 1.45 and Mach = 1.55 test points experiencing inlet planar wave, at off-nominal angle-of-attack and angle-of-sideslip. Baseline vortex generators, ECS bumps, and nose.
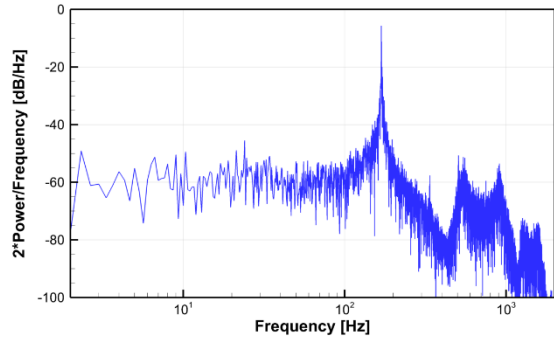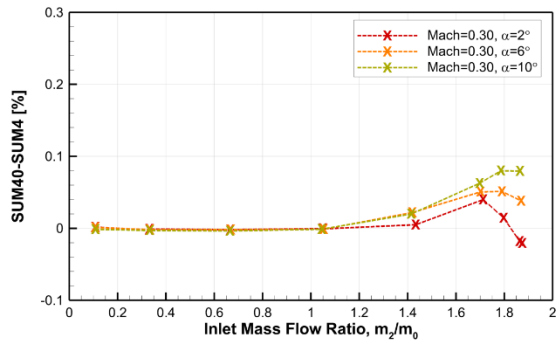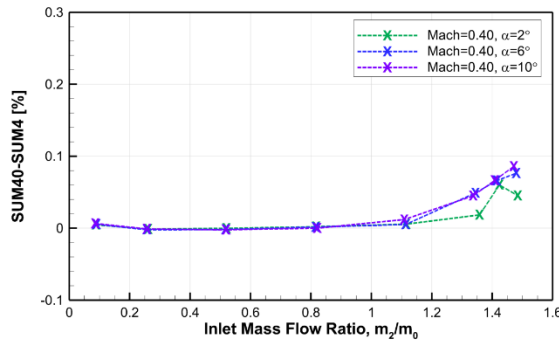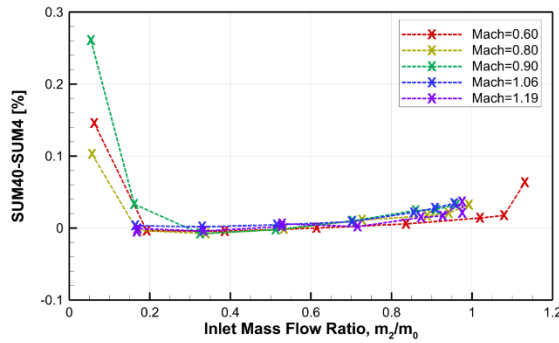
Figure 19.—Examples of power spectral density plots of Mach = 0.60 and Mach = 0.90 test points experiencing inlet planar wave. Baseline vortex generators, ECS bumps, and nose.

a) Mach=0.30, β=0°.

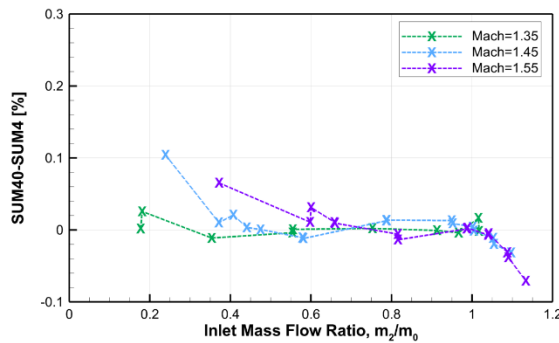**b) Mach=0.40, β=0°.**

c) Mach=0.60 to Mach 1.19, α=2°, β=0°.

d) Mach=1.35 to Mach 1.55, α=2°, β=0°.

Figure 20.—Sensitivity of SUM4 error (SUM40-SUM4) to variations in inlet mass flow ratio. Baseline vortex generators, ECS bumps, and nose.

3.6   Alternate Geometries

3.6.1   Alternate Vortex Generators

An alternate set of fuselage-mounted vortex generators (pictured in Figure 4(b)) was tested during the HSIDT. The alternate set of vortex generators, which were twice the height of the baseline vortex generators, were manufactured and tested in case the inlet performance using the baseline vortex generators was less than expected. Figure 21 and Figure 22 show the sensitivity of inlet distortion to variations in angle-of-attack and angle-of-sideslip, respectively, for each set of vortex generators. Only results for selected Mach and model attitudes are shown. At Mach = 0.30 (Figure 21(a) to (d) an Figure 22(a) to (b)), the alternate vortex geometry had little impact on circumferential and radial distortion. At Mach = 1.45 (Figure 21(e) to (h) and Figure 22(c) to (d)), the alternate vortex generator geometry had a bit more impact, reducing the high-response circumferential and radial distortion parameters by up to 1 percent for many of the model attitudes shown. At Mach = 1.45, $\alpha = 0°$, and $\beta = 1°$, the alternate vortex generators reduced the high-response circumferential distortion by 2 percent. The baseline vortex generator configuration already has inlet distortion within the engine's distortion limits, so the small reductions in inlet distortion produced by the alternate vortex generator configuration are not necessary from an inlet distortion perspective. With respect to inlet total pressure recovery, performance with the alternate vortex generators was generally as good as that with the baseline vortex generators. There were only small increases (less than 1 percent) over the baseline total pressure recovery at a few conditions (e.g., Mach = 1.45, $\alpha = 0°$, and $\beta = 1°$). While the alternate vortex generators may have had small improvements over the baseline vortex generators at some conditions, these small improvements must be weighed against any increased vehicle drag they may produce due to the additional height.

3.6.2   Environmental Control System Blank Inserts

As with the alternate vortex generators, the HSIDT also tested the model with the environmental control system (ECS) blanks in place, as shown in Figure 3(b). Since the ECS intakes and exhaust had been moved to the upper surface of the wing since the Inlet Performance Test, a goal was to assess the impact of the non-flowing ECS bumps on inlet performance for selected test conditions. Figure 23 and Figure 24 show the sensitivity of inlet distortion to variations in angle-or-attack and angle-of-sideslip, respectively, for the baseline non-flowing ECS bump inserts and the ECS blank inserts. Generally, the inlet distortion with the ECS blank inserts was similar to the inlet distortion with the baseline ECS bump inserts. In some conditions, the ECS blank inserts had a small increase in inlet distortion (less than 0.5 percent). There were no significant differences in total pressure recovery between the two ECS insert configurations at the conditions tested. Unfortunately, it was not possible to test and assess the impact of flowing ECS inlets and exhaust during the HSIDT.
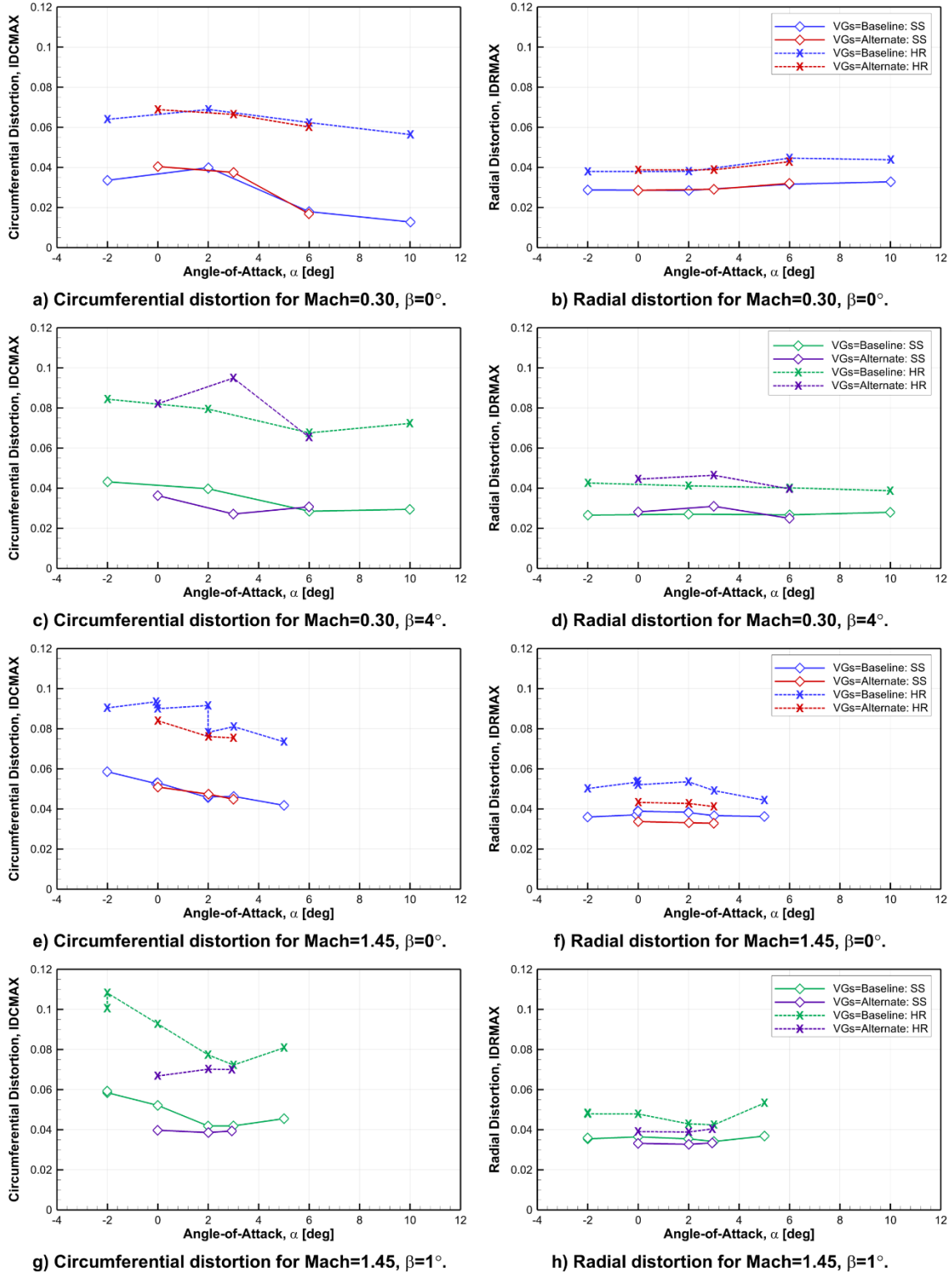
Figure 21.—Sensitivity of inlet distortion parameters to vortex generator (VG) configuration, shown for variations in angle-of-attack. Approximate maximum operating corrected inlet mass flow. Baseline ECS bumps, and nose.

a) Circumferential distortion for Mach=0.30, α=6°.

b) Radial distortion for Mach=0.30, α=6°.

c) Circumferential distortion for Mach=1.45, α=2°.

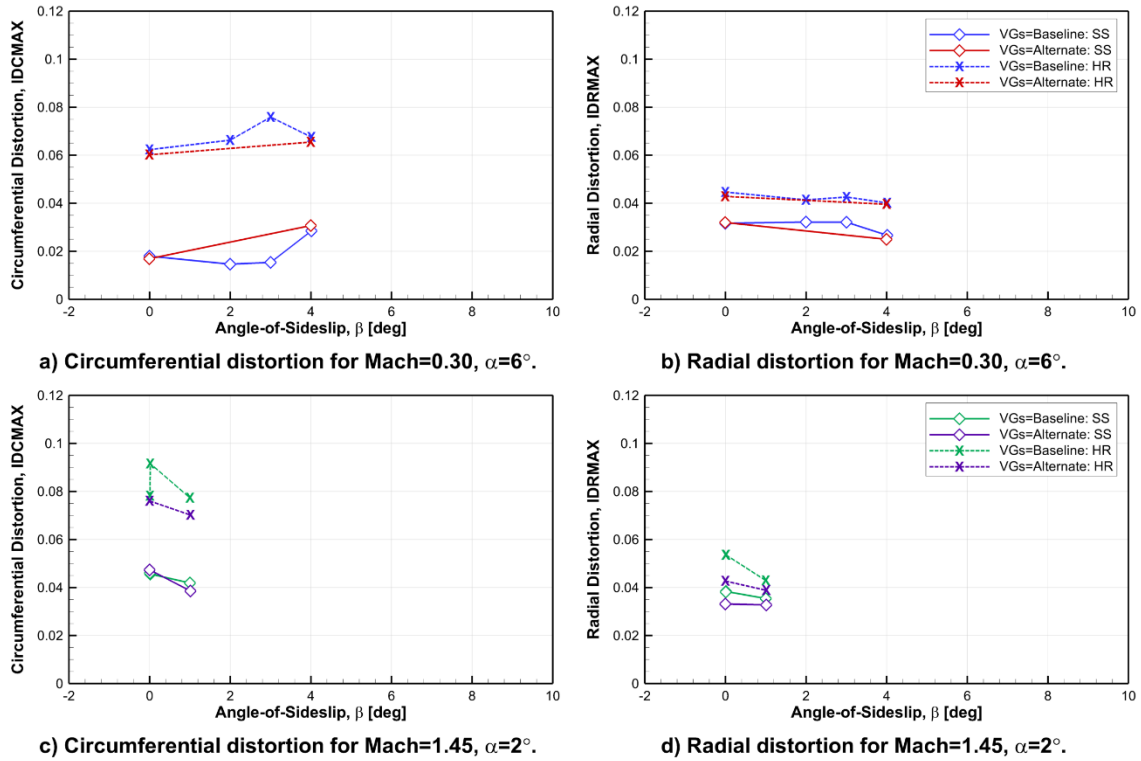**d) Radial distortion for Mach=1.45, α=2°.**

Figure 22.—Sensitivity of inlet distortion parameters to vortex generator (VG) configuration, shown for variations in angle-of-sideslip. Approximate maximum operating corrected inlet mass flow. Baseline ECS bumps, and nose.

a) Circumferential distortion for Mach=0.40, β=0°.

b) Radial distortion for Mach=0.40, β=0°.

c) Circumferential distortion for Mach=0.40, β=4°.

d) Radial distortion for Mach=0.40, β=4°.

e) Circumferential distortion for Mach=1.45, β=0°.

f) Radial distortion for Mach=1.45, β=0°.

g) Circumferential distortion for Mach=1.45, β=1°.

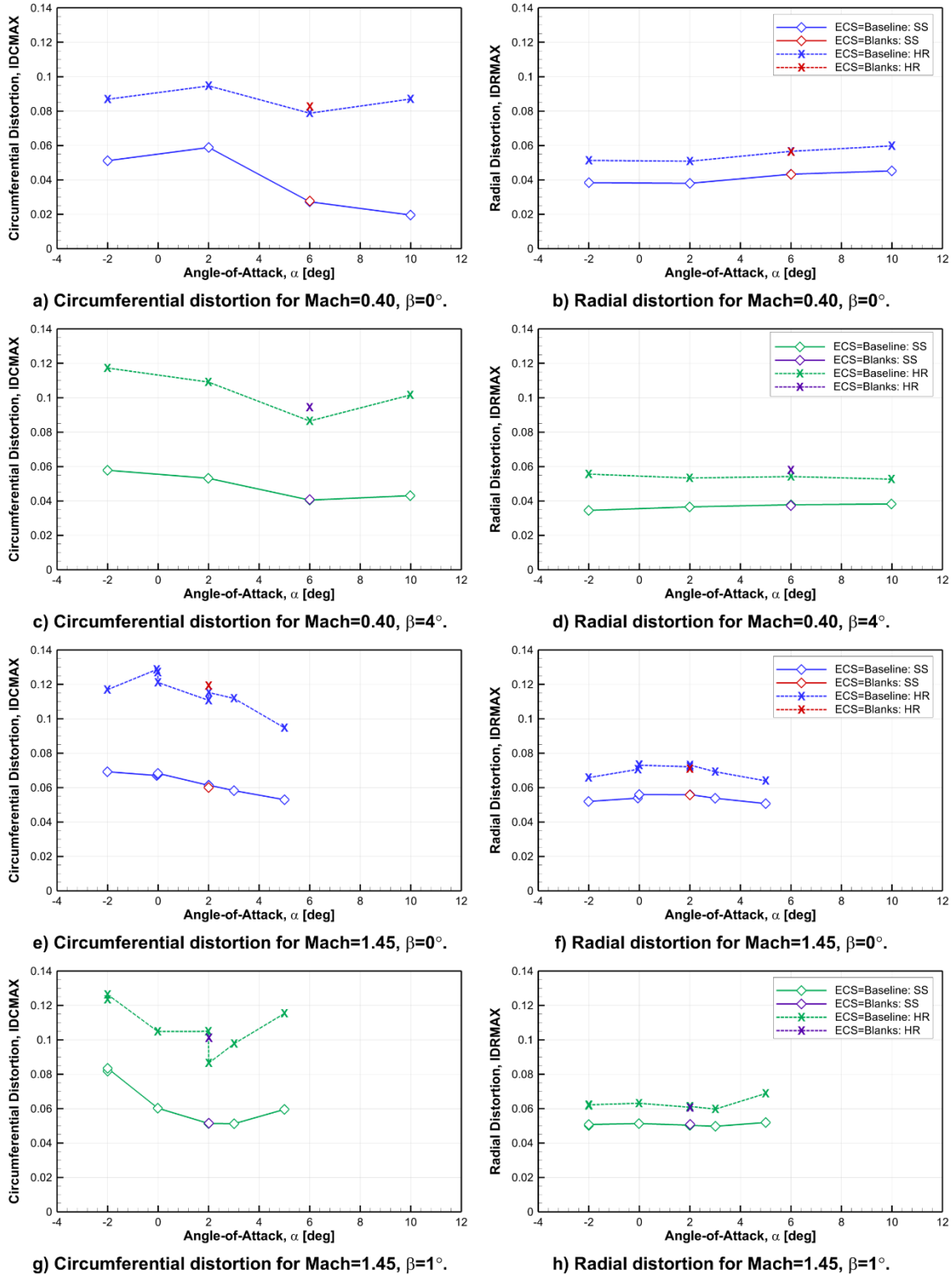**h) Radial distortion for Mach=1.45, β=1°.**

Figure 23.—Sensitivity of inlet distortion parameters to environmental control system (ECS) configuration, shown for variations in angle-of-attack. Approximate maximum operating corrected inlet mass flow. Baseline ECS bumps, and nose.
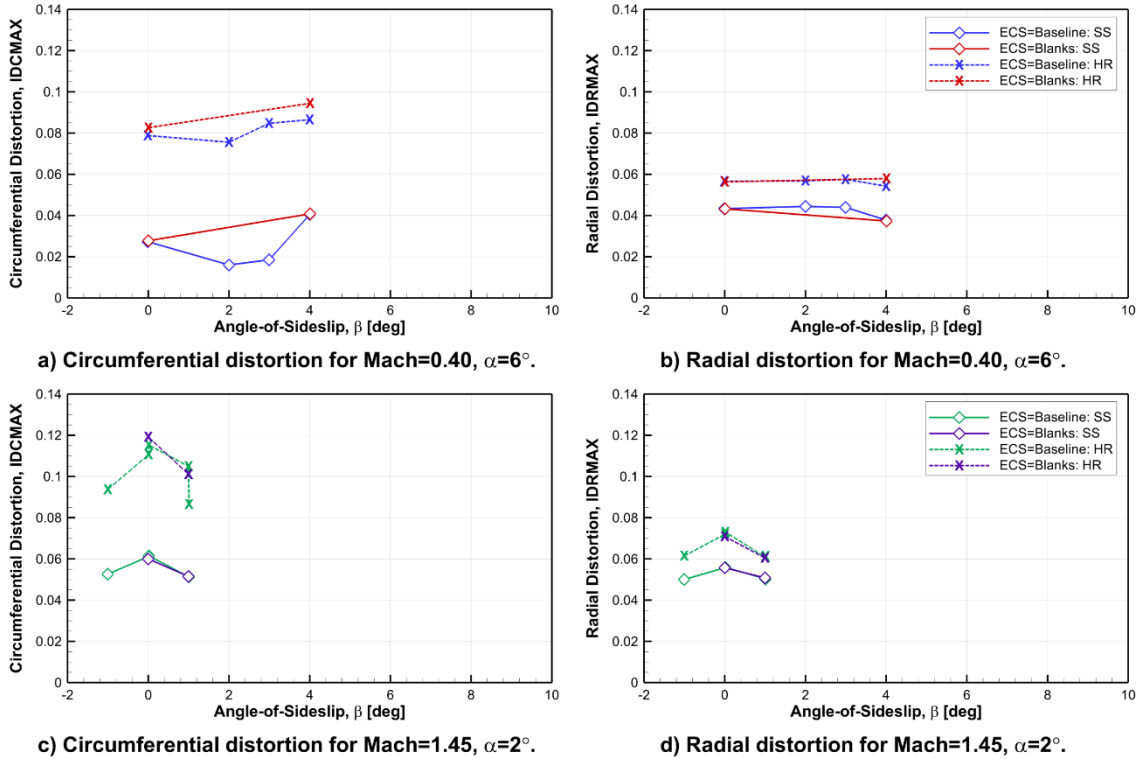
Figure 24.—Sensitivity of inlet distortion parameters to environmental control system (ECS) configuration, shown for variations in angle-of-sideslip. Approximate maximum operating corrected inlet mass flow. Baseline ECS bumps, and nose.

4.0 Conclusions and Recommendations

The X–59 High Speed Inlet Distortion Test (HSIDT) collected over 2,100 data readings for the 9.5 percent-scale QueSST propulsion model in the in the NASA Glenn Research Center 8- by 6-Foot Supersonic Wind Tunnel (8x6 SWT). These include over 1,700 data readings for the baseline configuration and approximately 400 data readings for alternative configurations. Both steady-state and dynamic data was collected for each reading. Inlet distortion data was collected using a 40-probe, area-weighted rake located at the inlet Aerodynamic Interface Plane (AIP). Each "probe" consisted of a steady-state pitot pressure probe and a high-response total pressure probe in a side-by-side arrangement.

The HSIDT confirmed the X–59 inlet/engine operability and compatibility within the operational envelope, with few exceptions. The HSIDT data showed that X–59 flight envelope for Mach = 0.3 to 1.19 is free of inlet planar wave (inlet buzz) and within dynamic distortion limits except at very low inlet air flows—airflows not expected during normal operation. At higher tunnel Mach numbers (Mach = 1.35 to 1.55), the test data showed that inlet distortion levels were within the distortion limits, but that the inlet could experience inlet planar wave at airflows lower than the full military power (maximum) engine airflow. Based on these findings, the X–59 will utilize speed lock-up to limit throttle back when decelerating from high flight Mach numbers to prevent the airflows that cause inlet planar wave.

The HSIDT also showed that there is a significant difference between steady-state distortion parameters and maximum instantaneous high-response (dynamic) distortion parameters. For the cases examined (multiple supersonic speeds, $\alpha = 2°$, $\beta = 0°$), the maximum instantaneous distortion parameters were up to twice as large as the steady-state values at high inlet mass flows and up to 100 times as large at low inlet mass flows.

The HSIDT showed that SUM4, computed from the four high-response inlet static pressure probes, consistently agreed with SUM40, computed from the 40 high-response AIP total pressure probes, within the X–59 operational envelope. Therefore, SUM4 can be used as a surrogate to indicate inlet planar wave during the X–59 flight test. Error ranged from –0.12 to 0.05 percent, but no clear correlation was found between error and Mach number, airflow, or attitude.

While circumferential and radial distortion were within limits for all the angle-of-attack and angle-of-sideslip ranges tested during the HSIDT, it is important to note that the tested ranges did not fully extend to the control law hard limits at every Mach number. It will be imperative for flight test engineers to monitor engine performance if the X–59 is tested at angles-of-attack and angles-of-sideslip that exceed the ranges tested during the HSIDT and fall within the control law hard limits. Likewise, flight test engineers will also need to monitor SUM4 at these angles-of-attack and angles-of-sideslip to reduce the possibility that of inlet planar wave at these vehicle attitudes.

The HSIDT compared inlet distortion and inlet total pressure recovery of the baseline vortex generator configuration and non-flowing environmental control system (ECS) bumps with an alternate vortex generator configuration and blank ECS inserts, respectively. The alternate vortex generator configuration produced some small reductions in inlet distortion and some small increases in inlet total pressure recovery, at a few conditions at high tunnel Mach numbers. This showed that there are few gains by using the taller alternate vortex generators over the shorter baseline vortex generators. When compared to model with the ECS blank inserts, the baseline ECS insert configuration showed that the non-flowing ECS bumps did not significantly impact the inlet distortion or total pressure recovery.

Beyond testing the inlet/engine compatibility and operability of the X–59, the 2019 High Speed Inlet Distortion Test built upon the successful 2017 Inlet Performance Test. The HSIDT added to the large data set from the prior test by collecting the first known high-response inlet distortion data of a full vehicle configuration for a top-mounted, centerline, diverterless bump inlet in a supersonic wind tunnel.

References

1. Castner, R. Simerly, S., Rankin, M., "Supersonic Inlet Test for a Quiet Supersonic Transport Technology Demonstrator in the NASA Glenn 8- by 6-Foot Supersonic Wind Tunnel," AIAA Paper 2018-2850, June 2018.
2. Soeder, R., "NASA Lewis 8- by 6-Foot Supersonic Sind Tunnel User Manual," NASA TM-105771, February 1993.
3. Stephens, J., Hubbard, E., Walter, J., McElroy, T., "Uncertainty Analysis of the NASA Glenn 8x6 Supersonic Wind Tunnel," NASA/CR—2016-219411, November 2016.
4. Arrington, A., "Calibration of the NASA Glenn 8- by 6-Foot Supersonic Wind Tunnel (1996 and 1997 Tests)," NASA/CR—2012-217270, January 2012.
5. Mitchell, G.A., "Blockage Effects of Cone-Cylinder Bodies on Perforated Wind Tunnel Wall Interference," NASA TM X-1655, 1968.
6. "Gas Turbine Engine Inlet Distortion Guidelines," SAE-ARP1420C, April 2017.
7. Arend, D.J., and Saunders, J.D., "An Experimental Evaluation of the Performance of Two Combination Pitot Pressure Probes," NASA/TM—2009-215632, October 2009.
8. Norby, W.P., "Small Scale Inlet Testing for Low Cost Screening Applications," AIAA-90-1926, July 1990.
9. "Inlet/Engine Compatibility – From Model to Full Scale Development," SAE AIR-5687-2011, September 2011.
10. Dippold, V.F., Castner, R.S., Friedlander, D.J., Heath, C.M., Heberling, B.C., Sozer, E., Endo, M., "Propulsion Flowpath Computational Fluid Dynamics Analyses of the X–59 QueSST in Support of Critical Design Review," NASA/TM-20205001430, September 2020.
11. "An Assessment of Planar Waves," SAE AIR5866, February 2008.